Reduced TBX5 dosage undermines developmental control of atrial cardiomyocyte identity in a model of human atrial disease

Irfan S. Kathiriya[1,2,#], Kavitha S. Rao[1,2], Alexander P. Clark[3], Kevin M. Hu[1,2,10], Zoe L. Grant[2], Megan N. Matthews[1,11], Zhe Chen[2], Swetansu K. Hota[2,12], Jeffrey J. Saucerman[3,4], Benoit G. Bruneau[2,5,6,7,8,#]

[1]Department of Anesthesia and Perioperative Care, University of California, San Francisco, USA, [2]Gladstone Institutes, USA, [3]Department of Biomedical Engineering, University of Virginia, USA;, [4]Robert M. Berne Cardiovascular Research Center, University of Virginia, USA;, [5]Roddenberry Center for Stem Cell Biology and Medicine, Gladstone Institutes, USA, [6]Cardiovascular Research Institute, University of California, San Francisco, USA, [7]Department of Pediatrics, University of California, San Francisco, [8]Institute of Human Genetics, University of California, San Francisco, [10]Current address: Creighton University School of Medicine, USA, [11] Current address: California Institute of Technology, Pasadena, CA, [12]Current address: Herman B. Wells Center for Pediatric Research, Indiana University School of Medicine, USA

[#]These authors jointly supervised this work.

Correspondence to I.S.K irfan.kathiriya@ucsf.edu or B.G.B. benoit.bruneau@gladstone.ucsf.edu

Abstract

While atrial septal defects (ASDs) and atrial fibrillation (AF) present differently, there is evidence that they share some genetic basis. Here, we used directed differentiation of human induced pluripotent stem cells into atrial or ventricular cardiomyocytes (CMs) to delineate gene regulatory networks (GRNs) that define each identity. We uncovered accessible chromatin regions, transcription factor motifs and key regulatory nodes specific to, or shared by, both CM types, including the transcription factor *TBX5*, which is linked to genetic susceptibility of ASDs and AF in humans. Complete *TBX5* loss resulted in a near absence of atrial CMs with a concomitant increase in the abundance of other cell types. Reduced dosage of TBX5 in human

atrial CMs caused cellular, electrophysiologic and molecular phenotypes consistent with features of atrial CM dysfunction. This included dose-dependent aberrant accessibility of many chromatin regions and perturbation of gene regulatory networks of atrial CM identity. These results suggest that, in addition to stemming from ion channel or extracellular matrix dysfunction, atrial diseases such as ASDs or AF may result from disruptions of atrial CM identity.

Introduction.

Thin-walled atria are distinct from thick-walled ventricles in their developmental origin and function. Atria serve to collect blood in the heart, initiate and propagate an electrical signal for coordinated cardiac contraction, and respond to physiologic changes such as heart failure by secreting hormones. These functions reflect the distinct phenotypes of atrial cells. For example, atrial fibroblasts display a greater response to pathologic stimuli than ventricular fibroblasts (Burstein et al., 2008), and atrial cardiomyocytes (CMs) display distinct electrophysiologic characteristics, calcium-handling and contractile proteins, cell-cell coupling and energy metabolism, which are reflected in human atrial gene expression *in vivo* (Dobrev et al., 2019).

Atrial disease is common and increases cardiovascular and cerebrovascular risk. Developmental defects of the atria include cor triatriatum, atrial aneurysms, patent foramen ovale (PFO) and atrial septal defects (ASDs). ASDs are one of the most common forms of congenital heart defects (CHDs), affecting 25% of the CHD population (Hoffman and Kaplan, 2002). Some large ASDs can lead to heart failure and require surgical repair. With aging, atrial tissue can manifest chaotic electrical activity known as atrial fibrillation (AF). AF is the most common arrhythmia and a leading cause of heart failure, stroke and sudden cardiac death (Kornej et al., 2020). Moreover, there is an increasing prevalence of AF in adults with CHDs, and AF risk is higher in patients with ASDs than in the non-CHD population (Miguel and Ávila, 2021). However, the molecular basis of ASDs and AF remains poorly understood, and new insights are needed to develop new diagnostic and therapeutic approaches.

There is ample evidence that atrial diseases share a genetic basis. ASDs are caused by inherited dominant mutations in genes encoding sarcomere proteins (Ching et al., 2005; Matsson et al., 2008; Postma et al., 2011), chromatin modifying enzymes (Boniel et al., 2021) and transcription factors (Basson et al., 1997; Garg et al., 2003; Kirk et al., 2007; Li et al., 1997; Posch et al., 2010; Schott et al., 1998; Yuan et al., 2013). Atrial fibrillation is associated with inherited mutations or variants in genes encoding potassium channels (Chen et al., 2003; Hong et al., 2005; Olson et al., 2006; Xia et al., 2005; Yang et al., 2004), but also sarcomere proteins (Choi et al., 2018; Gudbjartsson et al., 2016; Lee et al., 2018), and transcription factors (Guo et al., 2016; Ma

et al., 2016; Roselli et al., 2018; Xie et al., 2013). Thus, some genes associated with ASDs and AF may have overlapping functions, though the mechanisms underlying or linking the two atrial diseases are unclear.

Heterozygous mutations of the transcription factor *TBX5* cause Holt-Oram syndrome, a developmental disorder that often includes ASDs in humans (Basson 1997,Li 1997) and in mice (Bruneau et al., 2001). Conditional loss of *Tbx5* in the endocardium (Nadeau et al., 2010) or dorsal mesenchymal protrusion (Xie et al., 2012) leads to ASDs, suggesting an essential role for TBX5 in atrial septal development. Post-natal deletion of *Tbx5* in atrial CMs leads to AF via a calcium transport mechanism (Dai et al., 2019; Nadadur et al., 2016), and *Tbx5* was shown to be essential for the maintenance of an atrial gene expression program (Sweat et al., 2023). Some inherited *TBX5* mutations cause both ASDs and AF in the same individuals (Bever et al., 1996; Postma et al., 2008). As TBX5 is broadly associated with atrial gene regulation, ASDs and AF, understanding TBX5 function presents an opportunity to decipher the rules of gene regulation in atrial development and disease.

To model human atrial disease *in vitro*, multiple groups have developed methods that promote atrial CM differentiation of human pluripotent stem cells, garnering important insights into the pathways involved (Cyganek et al., 2018; Devalla et al., 2015; Lee et al., 2017; Yang et al., 2022a; Zhang et al., 2019). These protocols have been used on wild-type cells for cell type-specific drug screening (Devalla et al., 2015), and for inducing AF by electrical stimulation (Goldfracht et al., 2019) or with drugs that increase the risk of AF (Shafaattalab et al., 2019). However, human cellular models of genetic susceptibility to atrial disease have not yet been reported.

Here, we deployed a recently developed induced pluripotent stem cell (iPSC) model of Holt-Oram Syndrome (Kathiriya et al., 2021) to study genetic susceptibility to human atrial diseases. We observed disease-relevant cellular, electrophysiologic and molecular deficits of atrial CMs. The deficits in cell physiology and developmental gene expression were more profound than those previously observed in ventricular CMs lacking one or two copies of *TBX5* (Kathiriya et al., 2021). Notably, atrial CM specification failed in the complete absence of *TBX5* and atrial CM identity was hindered by heterozygous loss of *TBX5*. Furthermore, we discovered gene regulatory networks (GRNs) for atrial CM identity that were sensitive to TBX5 dosage, and observed disruptions to key nodes, including ASD- and AF-risk genes, in atrial disease-relevant networks.

Results.

99 Modeling atrial CM identity from human iPSCs delineates chamber-specific cellular attributes.

100 As an initial step to model atrial differentiation and disease, we differentiated wildtype (WT)
101 iPSCs (WTC11 parental line) (Miyaoka et al., 2014) into either atrial or ventricular CMs and
102 validated atrial-specific vs. ventricular-specific CM characteristics. Immunostaining showed ANP,
103 a well-known atrial marker, to be enriched in atrial CMs (Fig. 1A-G). By contrast, MLC2V, a
104 ventricular marker, was nearly absent among atrial CMs compared to ventricular CMs (Fig. 1H-
105 N). Multielectrode array (MEA) assays revealed a faster beat rate among atrial CMs and shorter
106 rate-adjusted local extracellular action potentials (LEAP), consistent with atrial CM
107 electrophysiology (Fig. 1O, P)(Nerbonne and Kass, 2005) and with iPSC-derived atrial CMs
108 derived by another protocol (Cyganek et al., 2018).

109 We then performed single-cell RNA sequencing (scRNA-seq) on atrial differentiation at
110 day 20 and merged it with previously generated scRNA-seq data of ventricular differentiation at
111 day 23 (Fig. S1A-C) (Kathiriya et al., 2021). Differential expression analysis confirmed that atrial
112 CMs were enriched for atrial genes (e.g. *TBX5*, *NR2F2, HEY1, MYH6*), the right atrial CM gene
113 *HAMP* (Litviňuková et al., 2020; Mir et al., 2023), the left atrial CM gene *PITX2* (Campione et al.,
114 2001; Kitamura et al., 1999; Liu et al., 2002; Schweickert et al., 2000) and the atrial appendage
115 CM gene *NPPA*, but did not express ventricular-specific genes (*MYL2*, *IRX4, HEY2, HAND1,*
116 *MYH7*) (Fig. 1Q, S1D-E, Table S1).

117

118 Human iPSC-derived atrial CMs display distinct epigenomic features.

119 We next compared accessible chromatin regions between differentiations to ventricular
120 and atrial CMs using single-nucleus ATAC sequencing (snATAC-seq) (Fig. S2A,B, Table S2). We
121 annotated cell type clusters by gene score using ArchR (Granja et al., 2020). Among *TNNT2*-
122 gene score$^+$ cells, representing presumptive CMs (Fig. S2B'), *MYL2*-gene score$^+$ clusters
123 overlapped with cells from ventricular CM differentiations and *MYH6*-gene score$^+$ clusters with
124 cells from atrial CM differentiations (Fig. S2C), as expected. Within a subset of *TNNT2*-gene
125 score$^+$ CMs (Fig. S2D,E), we found that accessible chromatin regions were distributed across
126 promoters, introns, exons and distal regions to a similar degree among clusters of ventricular or
127 atrial CMs (Fig. S2F).

128 By genomic coordinates, about one-quarter of accessible regions (42,108 regions)
129 overlapped between ventricular and atrial CMs at the stages assessed, out of 56,301 ventricular
130 CM-specific and 63,173 atrial CM-specific regions identified (Fig. 1R). Based on fold change
131 differences, we also identified 465 differentially accessible regions (DARs) among ventricular or

132 atrial CMs (Fig. S2G). Thus, although several accessible regions may be common to ventricular
133 and atrial CMs, the degree of accessibility may be different among ventricular or atrial CMs.
134 Among DARs, transcription factor (TF) motifs enriched among ventricular CMs included
135 MADS-box/MEF2 (Desjardins and Naya, 2016; Medrano and Naya, 2017; Naya et al., 2002),
136 TEAD (Gise et al., 2012; Lin et al., 2016) and NFAT (Bushdid et al., 2003) motifs (Fig. 1S). Atrial
137 CMs were enriched for NKX, NR2F, GATA and TBX or MEIS (Luna-Zurita et al., 2016) motifs
138 (Fig. 1S). Notably, TF motifs of TGIF, a TALE homeodomain protein associated with
139 holoprosencephaly that inhibits retinoic acid signaling (Bartholin et al., 2006) and represses Smad
140 signaling (Nakashima et al., 2018) were observed. However, any potential role for TGIF or TGIF-
141 like factors in atrial development would require experimental evaluation.
142
143 Gene regulatory networks uncover TF nodes of atrial CM identity.
144 Gene regulatory networks (GRNs) reveal a web of “nodes”, TFs that are important for
145 establishment and maintenance of transcriptional programs, and “edges”, which are gene targets
146 connected to their regulatory nodes, thus yielding more information than just changes to gene
147 expression. To uncover GRNs of human ventricular or atrial CM identity, we applied CellOracle,
148 a machine learning-based approach that builds cell type-specific GRNs using both gene
149 expression and chromatin accessibility data (Table S3) (Kamimoto et al., 2023). For each node,
150 we calculated “betweenness centrality”, which measures information flow through each node, and
151 “degree out centrality”, which measures the number of outgoing direct connections to edges for
152 any given node. By these measures, canonical chamber-specific TFs such as *HEY2* and *HAND1*
153 acted as predominant nodes in ventricular CMs, and *NR2F2* and *HEY1* in atrial CMs (Fig. 1T,U,
154 Fig. S3A-F). Notably, *HEY2*, *HES4* and *HEY1* are involved in Notch signaling, suggesting that the
155 Notch pathway is a regulator of both atrial and ventral CM identities. We also identified TFs that
156 are lesser known in the developing heart as nodes, including *E2F1* in ventricular CMs and *NR2F1*
157 and *PLAGL1* in atrial CMs.
158 Some TFs (e.g. *HEY2*, *HEY1*, *TBX5*) displayed connections in both ventricular and atrial
159 CM GRNs, although the nature of their connections changed depending on ventricular or atrial
160 CM context (Fig. 1T,U, Fig. S3A-F). For example, ventricular-enriched *HEY2* displayed both
161 higher betweenness and higher degree-out centrality in ventricular CMs (Fig. S3E,F), confirming
162 the importance of *HEY2* in a ventricular CM network. In turn, *HEY2* displayed connections with a
163 positive correlation (i.e. directly proportional between the TF node and a target edge), suggesting
164 that *HEY2* positively regulates some ventricular CM genes (Fig. S3G). By contrast, some *HEY2*
165 connections to atrial CM-specific targets reflected negative correlations (i.e. inversely proportional

166 between the TF node and a target edge), suggesting that *HEY2* inhibits some atrial CM genes
167 (Fig. S3H). Like *HEY2* in ventricular CMs, atrial-enriched *HEY1* also displayed both higher
168 betweenness and higher degree-out centrality in atrial CMs (Fig. S3E,F). Interestingly, most *HEY1*
169 connections reflected positive correlations in ventricular CMs (Fig. S3I, while many connections
170 in atrial CMs reflected negative correlations (Fig. S3J), suggesting that *HEY1's* role is likely more
171 complex than *HEY2's* in the atrial CM network. *TBX5* showed connections with positive
172 correlations in both atrial and ventricular CMs, some of which were overlapping, implying some
173 shared roles in both ventricular and atrial CM networks (Fig. 1V, W). Although there were more
174 direct connections to target edges in ventricular than atrial CMs, betweenness centrality for *TBX5*
175 was higher in atrial CMs (Fig. S3E), implying a more important role in atrial CMs.
176 As variants in *TBX5* are associated with ASDs and AF, we hypothesized that *TBX5* plays
177 a central regulatory role in human atrial CMs. To test this hypothesis, we used CellOracle
178 (Kamimoto et al., 2023) to perform *in silico* perturbation of *TBX5* in atrial CM differentiation. In the
179 normal condition, WTC11 cells generated mostly *MYH6*$^{+}$ atrial CMs, some *MYH7*$^{+}$ ventricular-like
180 CMs and *TNNT2*$^{+}$ *COL3A1*$^{+}$ CMs, which express extracellular matrix genes (CMEs) (Fig. 1X).
181 CellOracle analysis predicted that complete loss of *TBX5* during atrial CM differentiation would
182 hinder specification of atrial CM identity and instead lead toward other CM subtypes, such as
183 CMEs (Fig. 1Y).
184
185 <u>Reduction of TBX5 dosage impairs cellular features of atrial CMs</u>.
186 To confirm the CellOracle prediction, we leveraged a human disease model of *TBX5*
187 haploinsufficiency (Kathiriya et al., 2021). To this end, we differentiated to atrial CMs iPSCs
188 carrying a heterozygous (*TBX5*$^{in/+}$) or homozygous (*TBX5*$^{in/del}$) *TBX5* loss of function (LOF)
189 mutation, or their wildtype parental line (WTC11) (Kathiriya et al., 2021). Western blot confirmed
190 reduced levels of TBX5 in *TBX5*$^{in/+}$ cells and absence of TBX5 in *TBX5*$^{in/del}$ cells at day 20 of atrial
191 CM differentiation (Fig. S4A, B). While *TBX5*$^{in/+}$ cells differentiated to beating atrial CMs, *TBX5*$^{in/del}$
192 cells often had compromised CM differentiation efficiency and rarely produced beating CMs (Fig.
193 2A). Further, *TBX5*$^{in/del}$ atrial CMs could not be recovered beyond day 20, indicating a more severe
194 phenotype in atrial than ventricular CMs (Kathiriya et al., 2021).
195 Furthermore, loss of *TBX5* function led to dosage-sensitive sarcomere disarray and
196 increased cell size at day 20 of differentiation (Fig. 2B-F, Fig. S4C-E), indicating atrial CM
197 dysfunction. Notably, increased cell size in *TBX5*$^{in/+}$ atrial CMs was not observed previously in
198 *TBX5*$^{in/+}$ ventricular CMs (Kathiriya et al., 2021), again suggesting that atrial CMs are more
199 susceptible than ventricular CMs to reduced TBX5 dosage. Upon replating *TBX5*$^{in/+}$ cells for

micro-electrode array (MEA), we observed prolonged local extracellular action potentials (LEAPs) with a broad plateau phase (Fig. 2G-J), reminiscent of ventricular-like CM action potentials. This prolonged action potential was consistent with observations from mouse *Tbx5*$^{-/-}$ atrial CMs (Yang et al., 2017) and human *TBX5* heterozygous mutant ventricular CMs (Bersell et al., 2023; Kathiriya et al., 2021), albeit using different methods.

Complete loss of *TBX5* prevents the specification of atrial CMs.

To determine the gene expression changes that underlie the phenotypes of *TBX5*-deficient atrial CMs, we performed scRNA-seq on these cells at day 20 of atrial CM differentiation (Fig. 1K, Fig. S4F). A high-level annotation of cell type clusters identified *TNNT2*$^{+}$ CMs (WT 60.6% *TNNT2*, *TBX5*$^{in/+}$ 59% and *TBX5*$^{in/del}$ 0.4%), *DLK1*$^{+}$ or *DCN*$^{+}$ fibroblast-like cells, *EPCAM*$^{+}$ epithelial-like cells, *SERPINA1*$^{+}$ or *TTR*$^{+}$ endodermal population, *TOP2A*$^{+}$ dividing cells and *NEFM*$^{+}$ neural-like cells (Fig. 2L,M). Using a generalized linear mixed effects model, we tested genotype-specific differences in cluster memberships. Indeed, *TBX5*$^{in/del}$ cells were significantly enriched in non-CM clusters of fibroblasts and epithelial-like cells, with a concomitant loss of CMs (Fig. 2N, S4G). As cluster assignments can change with UMAP resolution, we also employed Milo, a program that tests differential abundance by assigning cells to partially overlapping neighborhoods on a k-nearest neighbor graph (Dann et al., 2022). This method also showed a statistically significant change in the abundance of CMs, fibroblasts, epithelial and neural-like cells for *TBX5*$^{in/del}$ (Fig. 2O, P). In contrast, cell type abundance was generally similar among *TBX5*$^{in/+}$ cells and WT cells at this resolution.

Reduced TBX5 dosage perturbs the molecular identity of several atrial CM subtypes.

Next, we evaluated *TNNT2*$^{+}$ clusters and defined CM subtypes (Fig. 3A-C). In WT CMs, we identified CM subtypes that were enriched for *MYH6*$^{+}$ expression, such as *PITX2*$^{+}$ left atrial (LA)-like CMs, *HAMP*$^{+}$ right atrial (RA)-like CMs, *NPPA*$^{+}$ atrial appendage-like CMs, *RSPO3*$^{+}$ atrioventricular (AV) CMs and a cluster lacking expression of LA- or RA-like markers, which we inferred as atrial precursor-like CMs by pseudotime analysis with Monocle 3 (Cao et al., 2019) (Fig. 3D). Other clusters that had relatively lower *MYH6*$^{+}$ expression included *MYH7*$^{+}$ ventricular-like CMs expressing ventricular-enriched genes (e.g. *IRX4, HEY2*), *COL3A1*$^{+}$ clusters expressing fibroblast genes (e.g. *COL1A1*, *FN*, *SOX4*, *TGFB2*), resembling CMs expressing extracellular matrix genes (CMEs) in developing mouse hearts (DeLaughter et al., 2016). We also observed a small *HBD*$^{+}$ hematopoietic-like cluster.

233 While similar numbers of total *TNNT2*$^{+}$ CMs were observed for WTC11 (9823 cells) and
234 *TBX5*$^{in/+}$ (9311 cells), only 59 *TNNT2*$^{+}$ CMs were observed from complete loss of *TBX5,* indicating
235 severely impaired atrial CM differentiation, including of most atrial CM subtypes (Fig. 3E, Fig.
236 S5A). *TBX5*$^{in/del}$ CMs were devoid of *NPPA*$^{+}$ appendage-like CMs and RA-like CMs but were
237 observed in CME and AV CM clusters. Further, only two atrial precursor-like CMs were observed
238 in *TBX5*$^{in/del}$, indicating an absence of proper atrial CM specification, consistent with *in silico*
239 predictions (Fig. 1X,Y).
240 Although heterozygous loss of *TBX5* cells were found among RA-like, LA-like and *NPPA*$^{+}$
241 atrial appendage-like CM clusters, *TBX5*$^{in/+}$ cells were reduced in numbers, implicating a
242 deficiency of proper atrial CM identity (Fig. 3E, Fig. S5A). Concomitantly, *TBX5*$^{in/+}$ cells were
243 enriched for CMEs and AV CMs, consistent with dosage-sensitive expansion of some atrial CM
244 subtypes with loss of others.
245 In addition, a spectrum of phenotypes from *TBX5* heterozygous mutant cells were
246 observed, with some remaining similar to WT cells, while others were found in a *TBX5*
247 heterozygous-predominant cluster (e.g. CME-1) (Fig. 3A,C,E). Such variability in cellular
248 phenotypes may be of clinical relevance, as many affected members of multi-generational families
249 of Holt-Oram Syndrome, and genetically-determined CHDs in general, express variations in
250 cardiac phenotypes (Basson et al., 1994; Benson et al., 1998; Benson et al., 2003; Garg et al.,
251 2003; Garg et al., 2005).
252
253 <u>ASD- and AF-risk genes are vulnerable to reduced TBX5 dosage.</u>
254 Complete loss of *TBX5* in atrial CMs led to reduced expression of 243 genes and
255 increased expression of 340 genes (Fig. 3F,H, Table S4). Heterozygous loss of *TBX5* resulted in
256 reduced expression of 283 genes and increased expression of 279 genes (Fig. 3G,H, Table S4).
257 Differentially expressed genes were significantly enriched for known AF-, ASD-, or CHD-risk or
258 causative genes (Fig. 3I-K, Table S5). For instance, in *TBX5* heterozygous mutant cells,
259 susceptible genes included 8 ASD (e.g. *TBX20, FGFR2, GLI3, KAT6B, PBX1*), 80 AF (e.g. *DES,*
260 *CAMK2D, ID1, VCAM1*) and 4 ASD and AF- (e.g. *PITX2, ACTC1, MYH7*) risk genes (Fig. 3L).
261 Further, dose-dependent genes dysregulated in both *TBX5* mutant genotypes (Fig. 3M) included
262 atrial-specific genes (e.g. *NR2F2*, *HEY1*), the right atrial CM gene *HAMP*, sarcomere genes (e.g.
263 *TNNC1*, *TNNT2*), ECM genes (e.g. *COL3A1*, *FN1*) and AV canal markers (e.g. *RSPO3*, *BMP2*).
264 Many genes could be further categorized as risk genes for ASDs (e.g. *NR2F2, JAG1*) (Ching et
265 al., 2005; McElhinney et al., 2002; Turki et al., 2014), AF (e.g. *NPPA*, *TECRL, TTN)* (Choi et al.,
266 2018; Devalla et al., 2016; Hodgson-Zingman et al., 2008; Lee et al., 2018), or both ASDs and

267 AF (e.g. *MYH6*) (Ching et al., 2005; Lee et al., 2018; Postma et al., 2008; Postma et al., 2011;
268 Roselli et al., 2018; Vad et al., 2020; Yuan et al., 2013).
269 As expected, many previously characterized TBX5 targets (e.g. *NPPA*, *MYH6, PITX2,*
270 *DES*) (Bruneau et al., 2001; Garg et al., 2003; Kathiriya et al., 2021; Ouwerkerk et al., 2021)
271 displayed TBX5 dose-dependent dysregulation. We also discovered new putative TBX5
272 downstream genes, genes such as *ANGPT1, NR2F1* and *MEG3* (Fig. 3F-H). Notably, *ANGPT1*,
273 with known roles in cardiac jelly homeostasis during atrial chamber morphogenesis (Kim et al.,
274 2018), was downregulated in *TBX5* mutant CMs, whereas *MEG3*, a positive regulator of cardiac
275 fibrosis (Piccoli et al., 2017) was downregulated in $TBX5^{in/+}$ and upregulated in $TBX5^{in/del}$ CMs. We
276 confirmed altered mRNA expression of *NR2F1, DES*, *ANGPT1* and *MEG3* in *TBX5* mutant atrial
277 CMs by fluorescent *in situ* hybridization (Fig. 4A-M).
278 To determine if disturbances from reduced TBX5 are exacerbated later in atrial CM
279 differentiation, we performed scRNA-seq at day 45 in $TBX5^{in/+}$ atrial cells. Both high-level cell type
280 annotations as well as CM subtypes were similar to those observed at day 20, with the addition
281 of $SHOX2^{+}$ pacemaker-like cells (Fig. S6A-G). Fewer $TNNT2^{+}$ CMs and more $POSTN^{+}$ fibroblasts
282 were observed among $TBX5^{in/+}$ at day 45 (Fig. S6D). Among CM subtypes at day 45, $HAMP^{+}$ RA-
283 like, and $PITX2^{+}$ LA-like CMs were reduced, while CME-2s and $MYH7^{+}$ ventricular-like CMs were
284 enriched (Fig. S4E-H). These results indicated that $TBX5^{in/+}$ cells persisted in their failure to
285 differentiate to some atrial CM subtypes, with deviation towards other atrial CM subtypes.
286 Moreover, by day 45, a population of non-atrial CMs, mainly fibroblasts and ventricular-like CMs,
287 expanded. Thus, at day 45, heterozygous loss of *TBX5* appeared analogous, albeit to a lesser
288 degree, to complete loss of *TBX5* at day 20.
289 Disease genes were also enriched among the 244 upregulated and 154 downregulated
290 genes in $TBX5^{in/+}$ CMs at day 45 (Fig. S6I). These included 6 ASD- , 72 AF-, and 5 ASD- and AF-
291 risk genes (Fig. S6J-M). A merged analysis of day 20 and day 45 CMs (Fig. S7A,B) revealed
292 genes dysregulated at both timepoints, including 3 ASD- (e.g. *NR2F2, GPC3, MEIS2*), 17 AF-
293 (e.g. *ANGPT1, NPPA, TNNT2, TNNI3*) and 2 ASD and AF- (e.g. *MYH7, ACTC1*) risk genes (Fig.
294 S7C).
295
296 <u>Atrial-enriched TF motifs are sensitive in TBX5-dependent chromatin accessibility.</u>
297 To evaluate whether altered chromatin accessibility might explain disturbances to gene
298 expression by reduced TBX5 dosage in atrial CMs, we performed snATAC-seq analysis of WT
299 and *TBX5* mutant cells at day 20 of atrial CM differentiation (Fig. 5A,B, Fig. S8A). Among *TNNT2*
300 gene $score^{+}$ clusters, cluster C5 was enriched for $TBX5^{in/del}$ cells, which showed reduced gene

301 scores for *MYH6*, *PITX2, HAMP* and *NPPA,* and increased gene scores for *COL3A1*, indicating
302 disrupted chromatin accessibility of CMs from complete *TBX5* loss. In contrast, cluster C6 was
303 enriched for *TBX5*$^{in/+}$ cells and displayed reduced gene scores for *PITX2*, *HAMP* and *NPPA*,
304 consistent with disturbed chromatin accessibility of atrial CMs from heterozygous loss of *TBX5*
305 (Fig. 5C, D, Fig. S8B).

306 We analyzed DARs from reduced TBX5 dosage for TF motif loss or enrichment. We found
307 a loss of atrial-enriched NKX, TBX or MEIS and TFIG motifs between WT-enriched and *TBX5*$^{in/del}$-
308 enriched clusters, and similar loss of NKX, TBX or MEIS, GATA, NR2F and TGIF motifs between
309 WT-enriched and *TBX5*$^{in/+}$-enriched clusters (Fig. 5E,F, S8C-E, Table S6). These TF motifs
310 suggested a broadly disturbed deployment of cardiac TFs determining atrial CM identity in *TBX5*
311 mutants. In contrast, TF motifs gained included non-heart associated NFI, ventricular and outflow
312 tract-associated HAND, and BMP-responsive SMAD motifs in *TBX5*$^{in/del}$ atrial CM and motifs for
313 the epicardial-associated WT1 in *TBX5*$^{in/+}$ atrial CMs (Fig. 5E,F). These changes suggested non-
314 atrial CM TFs had gained accessibility to CM chromatin, consistent with ectopic expression of
315 non-atrial CM genes (Fig 3H).

316 As TBX and MEIS motifs share sequence similarity (Luna-Zurita et al., 2016), we
317 evaluated DARs with predicted TBX or MEIS motifs. We observed that approximately 40-60% of
318 regions less accessible in *TBX5* mutant CMs contained TBX or MEIS motifs compared to about
319 20% of regions more accessible in *TBX5* mutant CMs (Fig. 5G), implying that TBX5 may be
320 necessary for open chromatin. Further, to assess if changes in chromatin accessibility could be a
321 direct effect of reduced TBX5 dosage, we overlaid TBX5 occupancy from TBX5 ChIP-seq in WT
322 cells (Grant et al., 2025) on changes to chromatin accessibility in *TBX5* mutants. We found that
323 50-60% of the regions less accessible in *TBX5* mutants overlapped with normal TBX5-binding
324 regions, whereas less than 5% of the more accessible regions did (Fig. 5G'). This observation
325 suggests that reductions in chromatin accessibility are likely a direct effect of reduced TBX5
326 binding to its target sites. Evaluation of chromatin accessibility near differentially expressed genes
327 showed correlations between gene expression and chromatin accessibility (Fig S8F-K). Some
328 examples of DARs across genotype-enriched clusters included the proximal promoter of the AF-
329 linked gene *NPPA* (Horsthuis et al., 2008), the nearby *NPPA-NPPB* super enhancer (Man et al.,
330 2021) (Fig. 5H), as well as the promoter of the novel TBX5 atrial CM target *NR2F1* (Fig. 5I).
331

332 <u>Loss of one *TBX5* copy abolishes TBX5 centrality and rewires atrial GRNs.</u>

333 We used CellOracle (Kamimoto et al., 2023) to infer GRNs of atrial CMs by *TBX5* genotype
334 and to understand how reduced TBX5 dosage perturbs network connections for human atrial CM

335 identity (Table S7). Decreasing TBX5 dosage reduced the total number of nodes from 1106 in
336 WT to 1028 in *TBX5*$^{in/}$ and 941 in *TBX5*$^{in/del}$ (Fig. S9A), with a concomitant increase in genotype-
337 specific edges from 900 in WT to 1436 in *TBX5*$^{in/+}$ and 1625 in *TBX5*$^{in/del}$ (Fig. S9B). Many network
338 connections displayed shifts from positive correlations to negative correlations (e.g. *NR2F1*,
339 *NKX2-5*, *HEY1, TCF21*) (Fig. 6A-C, Fig. S9C-F). Furthermore, a network comprised of upstream
340 TFs connected to TBX5 or CHD-, ASD- and AF-risk TFs susceptible to reduced TBX5 dosage
341 showed fewer unique edges (61 in WT, 47 in *TBX5*$^{in/+}$*,* 36 in *TBX5*$^{in/del}$) and total nodes (27 in WT,
342 25 in *TBX5*$^{in/+}$*,* 19 in *TBX5*$^{in/del}$) (e.g. ASD-risk *SMC3* lost in *TBX5*$^{in/+}$ and *TBX5*$^{in/del}$, *MEF2A* lost in
343 *TBX5*$^{in/+}$) (Fig. 6D-F). These results indicated that these networks are less complex when TBX5
344 dosage is reduced, implying a loss to a TBX5-dependent atrial CM program.

345 Several TFs showed dosage-sensitive reduction in centrality by betweenness or degree
346 out (Fig. 6G,H). *NR2F1* maintained many of its degree-out connections in *TBX5*$^{in/+}$ cells, but the
347 strength of correlations, if not their direction, was altered (e.g. AF-risk *ANGPT1*, *MYL7, ASD-risk*
348 *NR2F2, SELENOP*) (Fig. 6I). Other *NR2F1* connections were lost (e.g. *NDUFB9*, *NDUFS7,*
349 *ETFA, ARHGAP5, CDC42EP3*) or gained (e.g. *NES*, *PPP1R12B, KDELR, APOA1, CNN3*),
350 consistent with a reconfiguration of *NR2F1* connections in response to reduced TBX5.
351 Correspondingly, the degree-out centrality of *TCF21,* which was low in WTC11 CMs, dramatically
352 increased in *TBX5*$^{in/+}$ and *TBX5*$^{in/del}$ CMs (Fig. S9E)*,* suggesting an ectopic fibroblast-like network
353 in *TBX5* mutants, potentially in conjunction with an increase in connections of the fibroblast-
354 associated *TCF12* (Fig. S9F).

355 Moreover, *TBX5* lost both its betweenness and degree-out centrality in *TBX5*$^{in/+}$ GRNs
356 (Fig. 6G, H). This included loss of all 25 connections, including with the highest correlated gene
357 *PGAM1*, along with *BMP5,* AF-risk *NPPA*, and ASD- and AF-risk *MYH7* (Fig. 6J), consistent with
358 profound disturbances to *TBX5* connections from heterozygous loss of *TBX5* in atrial CMs.
359 Notably, some TBX5 dosage-sensitive edge genes that lost direct connections to TBX5 appeared
360 to form new connections with other transcription factors, including both positive and negative
361 regulators (Fig. 6K, Fig. S10A-C). For example, the TBX5-dependent edge gene *PNISR* gained
362 positive connections to the ASD- and AF-risk TF *NKX2-5* and the cardiopulmonary disease-linked
363 TF *TBX4* (Prapa et al., 2022) in *TBX5*$^{in/del}$ CMs (Fig. S10B). Concurrently, *PNISR* showed
364 reduced strength of a negative connection to the disease-risk TF *TBX2* (Liu et al., 2018) in
365 *TBX5*$^{in/+}$*,* while gaining a positive connection to *TBX2* in *TBX5*$^{in/del}$ CMs (Fig. S10B). This
366 suggested some degree of buffering or compensation, albeit incomplete, by other TFs in the
367 setting of reduced TBX5 dosage. In sum, we found that reduced TBX5 dosage results in a

368 reconfiguration of atrial CM networks, including disruptions to connections of ASD- and AF-risk
369 genes.
370
371 **DISCUSSION**.
372 This study describes a human cellular model of TBX5-associated atrial disease and
373 reveals dosage-sensitive disruptions to atrial CM GRNs. Our findings uncover vulnerabilities in
374 atrial CM identity and provide further evidence that ASDs and AF share a molecular basis. These
375 insights advance our understanding of genetic susceptibility to atrial diseases and provide new
376 potential avenues for therapeutic development.
377 Using human differentiation systems to CMs, we discern epigenetic differences between
378 closely related cell types, ventricular and atrial CMs. These results provide further support that
379 these approaches may be useful to model *in vitro* cardiac diseases that affect one cell type versus
380 the other. For example, iPSC-derived ventricular CMs have been valuable to model susceptibility
381 to ventricular-specific diseases, such as hypertrophic or dilated cardiomyopathy, ventricular
382 arrhythmias, or congenital heart defect networks (Briganti et al., 2020; Friedman et al., 2024;
383 Hinson et al., 2015; Hnatiuk et al., 2021; Kathiriya et al., 2021; Knollmann, 2013; Lan et al., 2013;
384 Seeger et al., 2019; Sinnecker et al., 2013; Smith et al., 2018; Sun et al., 2012). Similarly, human
385 iPSC-derived atrial CMs can be leveraged for modeling AF, ASDs or other atrial diseases, and to
386 uncover atrial-relevant disturbances to GRNs and cellular physiology. In turn, human cellular
387 models of atrial disease could be used to screen drugs for therapeutic potential, teratogenicity,
388 and atrial arrhythmia risk, and to decipher non-coding variants or oligogenic inheritance of human
389 atrial diseases.
390 From our data, modeling GRNs of atrial or ventricular CM identity predicted key nodes
391 that could be critical for disrupting atrial GRNs. One of these key nodes is *TBX5*, which we and
392 others have studied (Bersell et al., 2023; Karakikes et al., 2017; Kathiriya et al., 2021). Here, we
393 have modeled reduced dosage, including absolute deficiency of *TBX5 in silico* and *in vitro*, in
394 human atrial cells. Based on changes in gene expression and chromatin accessibility, we have
395 inferred exquisitely sensitive GRNs that are important for atrial function and identity. It is
396 particularly striking that direct connections of multiple key nodes, such as *NR2F1* and ASD-risk
397 *NR2F2*, are affected within these dosage-vulnerable networks even from partial loss of *TBX5*,
398 leading to a cascading effect on susceptible downstream genes related to atrial CM identity.
399 Conversely, the gain of connections of fibroblast-associated *TCF21* and *TCF12* may reflect a
400 change in CM cell identity to CMEs, which express some fibroblast-like genes. In the setting of
401 genetic susceptibility to AF, for example, this perturbation of cell identity may contribute to an

402 atrial fibrosis-like state associated with AF (Platonov, 2017). For some Holt-Oram syndrome
403 patients, we speculate that in atrial tissue, the number of fibroblasts could be increased, while
404 CMEs could be expanded at the expense of other atrial CM subtypes.

405 Some nodes in the GRNs that define atrial CM identity are associated genetically with AF
406 and/or ASDs, suggesting a common disease network that may underly their pathologies. These
407 disrupted networks point to new TBX5-sensitive candidate genes, such as *NR2F1*, *ANGPT1* and
408 *MEG3*, and their biological processes as possible leads for therapeutic potential. Moreover,
409 reverting dosage-sensitive perturbations to more "normal" GRNs may offer therapeutic
410 opportunities to restore proper atrial identity in patients with genetic or acquired atrial conditions,
411 as demonstrated in another cardiovascular disease context (Theodoris et al., 2020). By combining
412 computational modeling with analysis of this cellular disease model, predictions to enhance TBX5
413 activity or improve disturbed atrial GRNs could be tested to mitigate atrial disease susceptibility
414 by small molecules or gene editing.

415 In conclusion, our discovery of a broad disruption to the GRNs underlying atrial identity in
416 the context of genetic susceptibility to atrial disease suggests that some atrial diseases, such as
417 ASDs or AF, may not only arise from disturbances of certain functional proteins, such as ion
418 channels or extracellular matrix components. Rather, some atrial diseases may be caused by a
419 fundamental disruption of atrial CM identity. More generally, we propose that perturbations to cell
420 identity may serve as a basis for genetic susceptibility underlying some human diseases.

421

422 **STUDY LIMITATIONS**. Several limitations of this study should be considered. Although this
423 human cellular model mimics certain disease phenotypes, ASDs and AF manifest in a 3-
424 dimensional tissue and cannot be fully recapitulated in a 2-dimensional model system. Moreover,
425 certain *in vivo* cell types may be missing or represented poorly *in vitro*. Likewise, contributions
426 from the spatial organization of cells *in vitro* or in heart tissue *in vivo* are not captured. Given that
427 there are several sub-categories of ASDs (e.g. primum ASD, secundum ASD, sinus venosus
428 ASD, or coronary sinus ASD) or AF (e.g. persistent AF, paroxysmal AF, or post-operative AF), it
429 remains to be determined how well this cellular disease model may reflect these conditions.
430 Further, by using scRNA-seq and snATAC-seq separately, we uncovered correlations between
431 gene expression and chromatin accessibility, rather than directly linking gene expression to
432 chromatin accessibility in the same cells. Finally, scRNA-seq data is currently available from LV
433 tissue from a Holt-Oram Syndrome patient (Steimle et al., 2024) but not from atrial tissue. As a
434 result, we cannot determine how many of our findings in our iPSC-derived atrial CM model of
435 Holt-Oram Syndrome will be valid in atrial tissue from some Holt-Oram syndrome patients.

436

437 **METHODS**.

438 **iPSC culture and atrial cardiomyocyte differentiation**. In accordance with the Human Gamete,
439 Embryo and Stem Cell Research (GESCR) Committee, which serves as the Stem Cell Research
440 Oversight Committee at UCSF, human iPSCs (WTC11, *TBX5*$^{in/+}$ and *TBX5*$^{in/del}$) (Kathiriya et al.,
441 2021) were maintained in mTESR Plus medium (Stemcell Technologies, 100-0276). For directed
442 differentiations, iPSCs were passaged on to GFR Matrigel-coated 6-well plates until 70%
443 confluency and then differentiated according to manufacturer's instructions using the Stemdiff
444 Atrial Cardiomyocyte Differentiation Kit (StemCell Technologies, 100-0215). iPSCs were
445 authenticated by genotyping for *TBX5* after each thaw of cells and tested for mycoplasma
446 contamination quarterly.

447

448 **Immunostaining**. Differentiated cells at day 20 from WTC11, *TBX5*$^{in/+}$ and *TBX5*$^{in/del}$ iPSCs were
449 dissociated using 0.25% trypsin and quenched with cardiomyocyte maintenance medium
450 containing 10% FBS. Cells were resuspended in cardiomyocyte maintenance medium with 10μM
451 ROCK inhibitor (StemCell Technologies, Y-27632), counted and plated onto growth factor-
452 reduced basement membrane matrix (GFR) Matrigel (Corning, 356231) coated-chambered slides
453 (Ibidi, 80381). Medium was replaced after 24 hours with fresh cardiomyocyte maintenance
454 medium. On the following day, cells were fixed in 4% formaldehyde for 15 minutes and washed
455 with PBS. Cells were then incubated in blocking buffer containing 5% goat serum and 0.1% Triton
456 X-100 in PBS for 1 hour at room temperature. Primary antibodies (alpha actinin, Sigma-Aldrich
457 Cat# A7811, RRID:AB_476766, 1:250 (King et al., 2011); MLC2V, Abcam Cat# ab79935,
458 RRID:AB_1952220, 1:200 (Yang et al., 2022a); ANP, GeneTex, GTX109255, 1:250 (Nandi et al.,
459 2021); cTNT, Thermo, Cat#MS-295-P, RRID:AB_61808, 1:500 (Kathiriya et al., 2021)) in blocking
460 buffer were incubated with cells for 2 hours at room temperature. Following washes in blocking
461 buffer, cells were incubated in secondary antibodies at 1:200 dilution (goat anti mouse Alexa Fluor
462 488, ThermoFisher, A11029, goat anti mouse Alexa Fluor 594, ThermoFisher, A11005). Cells
463 were then washed with blocking buffer and stained with DAPI at a 1:1000 dilution for 2 minutes.
464 Images were acquired using an Olympus FV3000RS and processed with ImageJ. Evaluations of
465 sarcomere disarray or cell size was performed as described previously (Kathiriya et al., 2021) at
466 day 20.

467

468 **Replating for multi-electrode array (MEA)**. iPSC-cardiomyocytes were harvested as described
469 above. An 8uL droplet of GFR Matrigel in KO DMEM was placed in the center of each well of a

470 BioCircuit MEA Plate (Axion Biosystems, M384-BIO-24) and incubated for 2 hrs at 37C. GFR was
471 gently removed and approximately 50,000 cells in 8-10ul droplets was placed in the center of
472 each well and incubated for 1 hr at 37C. After incubation, additional StemDiff maintenance media
473 with ROCKi was added to each well and incubated for 24 hrs at 37C. Subsequent media changes
474 were performed every other day with StemDiff maintenance media. MEA recordings were
475 acquired after at least 7 days of maintenance.
476
477 **MEA Electrophysiology**. Electrophysiological data was recorded on the Maestro Edge Micro
478 Electrode Array device (Axion Biosystems). Live recordings of iPSC-cardiomyocyte field
479 potentials and local extracellular action potentials (LEAPs) were acquired using the Cardiac
480 module in the AxIS Navigator Tool. Representative field potential and LEAP tracings from
481 recordings were acquired using the Axion Biosystems Cardiac Analysis Tool. Data collection and
482 analysis was performed using the MEA software (Axion Biosystems) according to manufacturer
483 instructions.
484
485 **Fluorescent *in-situ* hybridization**. iPSC-derived cardiomyocytes were harvested as described
486 above. Approximately 100,000 cells were then plated on to 3-well chambered slides with
487 removable silicone (Ibidi 80381). Cells were then fixed with 10% neutral buffered formalin for 30
488 minutes at room temperature, followed by washes with 1X PBS. Serial dehydration with 50%,
489 70% and 100% ethanol was performed, and slides were stored in 100% ethanol at -20C. On the
490 day of staining, cells were serially rehydrated and pretreated with hydrogen peroxide for 10
491 minutes and protease III for 10 minutes at a 1:5 dilution ratio. RNAscope Multiplex Fluorescent
492 Reagent Kit v2 (Advanced Cell Diagnostics, 323100) was used to detect *TNNT2* (518991),
493 *ANGPT1* (482901-C2), *DES* (403041-C2), *MEG3* (400821) and *NR2F1* (583751). Finally, silicone
494 chambers were removed from slides, and a coverslip was mounted using Prolong Gold anti-fade
495 mountant. Slides were imaged at 40X magnification on an Olympus FV3000RS confocal
496 microscope and analyzed using FIJI.
497
498 **Harvesting cells for single-cell RNA and ATAC sequencing**. Human iPSCs from WTC11,
499 *TBX5*$^{in/+}$ and *TBX5*$^{in/del}$ were differentiated using the Stemdiff Atrial Cardiomyocyte Differentiation
500 Kit (Stemcell Technologies 100-0215) or the Stemdiff Ventricular Cardiomyocyte Differentiation
501 Kit (Stemcell Technologies 05010). For atrial differentiations, two biological replicates of cells
502 were harvested from all three genotypes at day 20 for scRNA-seq (20,000 cells) or snATAC-seq
503 (10,000 cells), or from WTC11 and *TBX5*$^{in/+}$ at day 45 for scRNA-seq (20,000 cells), in separate

504 batches according to manufacturer instructions (10X Genomics). For ventricular differentiations,
505 two biological replicates of 10,000 cells were harvested at day 23 for snATAC-sequencing. Cells
506 were dissociated using 0.25% trypsin, quenched with cardiomyocyte maintenance medium
507 containing 10% FBS and then counted. Cell suspensions were processed for single-cell RNA
508 sequencing using Chromium Next GEM Single Cell 3' GEM, Library & Gel Bead Kit v3.1 (10X
509 Genomics). For single nuclei ATAC-sequencing, nuclei were harvested and processed according
510 to manufacturer's instructions using the Chromium Next GEM Single Cell ATAC Library & Gel
511 Bead Kit v1.1 (10X Genomics). Libraries were sequenced on an Illumina Novaseq6000 S4 or
512 Novaseq X.
513
514 **Analysis of single-cell RNA sequencing data**. Fastq files were processed using Cellranger
515 count (v6.1.1). Counts from samples from a single timepoint were aggregated using Cellranger
516 aggr without read-depth normalization. Seurat (v4.4) (Hao et al., 2021) was used to analyze the
517 data. Cells with low UMI count plus a high percentage of mitochondrial reads were considered
518 dying and removed. Potential doublets with aberrantly high gene counts were also removed. In
519 the day 20 dataset, cells with UMI counts between 4000-100,000 and gene counts between 500-
520 10,000 were retained. In the day 45 dataset, cells with UMI counts between 4000-50,000 and
521 gene counts between 500-8,000 were retained. Normalization was performed using SCTransform
522 and batch effects were corrected using the SeuratWrapper function RunHarmony. After
523 annotating major cell types, *TNNT2*$^{+}$ clusters were subset and further analyzed. Differentially
524 expressed genes with an adjusted $p<0.05$ from Wilcoxon rank-sum test were reported.
525
526 Metrics for cell quality control. After excluding cells that did not pass these quality control metrics,
527 we found that one cluster, at both days 20 and 45, was marked by CM genes (*TTN, TECRL,*
528 *MYH7B)*, as well as by many mitochondrial genes (*SLC25A37, MT-ND1, MT-ND4, MT-ND2, MT-*
529 *ATP6, MT-ND3, MT-CYB, MT-ND6, MT-ND5, MT-CO2, MT-CO3, MT-CO1, MT-ND4L*). As this
530 could be an indicator of CMs undergoing apoptosis, we excluded this cluster from downstream
531 analysis.
532
533 In Figure 1, single cell RNA sequencing data from WT atrial differentiation was merged
534 and analyzed with previously generated data from WT ventricular differentiation (Kathiriya et al.,
535 2021). Differentially expressed genes were obtained by comparing atrial CM clusters with
536 ventricular CM clusters. In Figure 3, WT cells from clusters highly enriched for *MYH6* were

537 compared to *TBX5*$^{in/+}$ or *TBX5*$^{in/del}$ cells from other clusters with *MYH6*, similar to the Monocle
538 partitions in Figure 3D.
539 Volcano plots were generated using the EnhancedVolcano package. Differential genes
540 were intersected with curated lists containing CHD-associated genes, atrial fibrillation-risk genes
541 and genes associated with atrial septal defects. CHD-associated gene list includes our previously
542 curated list from Kathiriya et al., 2021, and genes from the CHDgene database
543 (http://chdgene.victorchang.edu.au/) (Yang et al., 2022b). Atrial fibrillation-risk genes were
544 gathered from the Harmonizome database (https://maayanlab.cloud/Harmonizome/), and
545 (Ouwerkerk et al., 2019; Ouwerkerk et al., 2020; Roselli et al., 2018) (Table S5). The MiloR
546 package (v2.0.0) (Dann et al., 2022) was used for differential cell type abundance testing. The
547 precomputed KNN graph from Seurat was imported using the buildFromAdjacency function. The
548 number of nearest neighbors k was set to 40. Differential abundance results were visualized by
549 setting alpha = 0.05. Monocle 3 (v1.3.7) (Cao et al., 2019) was used for pseudotime analysis. A
550 separate Monocle 3 object was made for WTC11 or *TBX5*$^{in/+}$ cells, and a pseudotime trajectory
551 was generated for cells in partition 2. Cells in the atrial precursor-like clusters were chosen as
552 root cells for each Monocle 3 partition using the "order_cells" function. Pseudotime was visualized
553 on the UMAP using the "plot_cells" function.
554
555 **Cell abundance testing.** A Generalized Linear Mixed Effects Model (GLMM) was implemented
556 in the lme4 (version 1.1-37) R package (Bates et al., 2015) and was used to estimate the
557 associations between cell type-annotations and *Tbx5* genotype (WT, Het or Hom). These models
558 were run separately for each cluster of cells identified within the full data or within subtypes of
559 CMs. The family argument was set to the binomial probability distribution for the GLMM model fit.
560 Cluster membership of cells by sample was modeled as a response variable by a two-dimensional
561 vector representing the number of cells from the given sample belonging to and not belonging to
562 the cluster under consideration. The corresponding sample ID from which the cell was derived
563 was the random effect variable, and the genotype was included as the fixed variable. The resulting
564 P values for the significance estimated log odds ratios were adjusted for multiple testing using the
565 Benjamini–Hochberg method (Benjamini and Hochberg, 1995).
566
567 **Analysis of single-cell ATAC sequencing data**. Fastq files were processed using Cellranger
568 ATAC count (v2.0). Data was analyzed by following the tutorial for ArchR (v1.0.2) (Granja et al.,
569 2021). Cells with TSS enrichment >= 6 and nFrags >= 1500 were retained. Pseudobulk replicates
570 for each genotype in each cluster were generated with a minimum of 500 and maximum of 1000

571 cells for each replicate in a sample-aware manner. Peaks were called with MACS2 by setting
572 reproducibility to 2. Volcano plots show differential peaks with FDR < 0.1 and log2FC >0.25. Motif
573 annotations were added from CIS-BP repository using the addMotifAnnotations function and motif
574 enrichment in differential peaks was performed using the peakAnnoEnrichment function with FDR
575 <0.1 and log2FC >0.25. Overlapping ATAC (this manuscript) and TBX5 ChIP peaks (Grant et al.,
576 2025) were attained using findOverlaps from the Genomic ranges package. Browser tracks were
577 generated using IGV Desktop application. In Figure 1, differentially accessible regions were
578 reported between atrial CM clusters and ventricular CM clusters. In Figure 5, differentially
579 accessible regions were reported between WT cells in WT-enriched (C2+C3) clusters and
580 *TBX5*$^{in/+}$ cells in *TBX5*$^{in/+}$-enriched (C6) clusters or *TBX5*$^{in/del}$ cells in *TBX5*$^{in/del}$ -enriched (C5)
581 clusters.
582
583 **Gene regulatory network analysis**. Gene regulatory network analysis was performed using the
584 CellOracle (v0.18.0) package (Kamimoto et al., 2023). Default parameters were used according
585 to the documentation, unless specified otherwise. For wildtype atrial CM- and ventricular CM-
586 specific GRNs, base GRNs were constructed using scATAC-seq data at day 20 from WTC11
587 atrial CM and ventricular CM subsets, respectively (Table S3). Cell type-specific GRNs were then
588 constructed by setting alpha = 1000. For *TBX5* genotype-specific GRNs, base GRNs were
589 constructed using scATAC-seq data at day 20 from WTC11 cells (Table S7). The apparent
590 upregulation of *TBX5* mRNA presumably from non-mutated exons (Kathiriya 2021) in *TBX5*
591 heterozygous mutants was manually corrected by halving the raw counts in *Tbx5*$^{in/+}$ and setting
592 the raw counts to zero in *Tbx5* $^{in/del}$ cells, consistent with Western blot data (Fig S1A, B). Cell type-
593 specific GRNs were then constructed by setting alpha = 1000.
594 Inferred GRNs were filtered to include only the 12,000 edges with largest absolute
595 coefficient values. Centrality calculations for the 12,000 edge networks were calculated using
596 CellOracle's links.get_network_score() function. PyVis (Perrone et al., 2020) was used to
597 visualize subnetworks. The large nodes in these networks were manually selected TFs and small
598 nodes are the direct targets in the 12,000-edge networks. The edge color was selected to indicate
599 whether a TF activated (grey) or inhibited (red) a target, and edge thickness was scaled based
600 on absolute coefficient magnitude. For networks in (Fig 1T, U), we chose canonical atrial or
601 ventricular TFs, along with some novel TFs - *TBX5, NR2F2*, *MEF2C*, *NKX2-5*, *MEIS2*, *GATA4*,
602 *HAND1*, *IRX4*, *HEY2*, *PLAGL1*, *NR2F1*, *HES4*, *E2F1*, and *HEY1*. For networks in Fig 6A-C, the
603 manually selected TFs included *TBX5*, *NR2F2*, *MEF2C, NKX2-5, MEIS2, GATA4, HAND1, IRX4,*
604 *HEY2, PLAGL1, NR2F1, HES4, E2F1, HEY1, TCF21, TEAD1*, and *TCF12.* For Fig 6D-F, we

identified TFs that had source or target connections to TBX5 (Table S7) and prioritized ones that displayed dose-dependent change in centrality by *TBX5* genotype and are CHD- or AF- risk genes. These networks exclude the TFs and only show direct connections between prioritized genes. Wheel diagrams that display direct interactions between TFs and their targets were developed using Python's NetworkX package (Hagberg et al., 2008), with a circular layout and edge widths scaled by coefficient values.

ACKNOWLEDGEMENTS. We thank members of the Bruneau and Kathiriya labs for discussion and comments, and of the Gladstone Stem Cell Core, Histology and Microscopy, and Flow Cytometry Core and the UCSF Center for Advanced Technologies for their expert assistance. We thank Reuben Thomas of the Gladstone Bioinformatics Core for valuable feedback on statistical analyses, and Francoise Chanut of Gladstone Communications for editorial assistance. The Gladstone Flow Cytometry Core is funded by NIH S10 RR028962, the James B. Pendleton Charitable Trust and DARPA. Sequencing was performed at the UCSF CAT, supported by UCSF PBBR, RRP IMIA, and NIH 1S10OD028511-01 grants.

COMPETING INTERESTS. B.G.B. is a co-founder and shareholder of Tenaya Therapeutics, and none of the work presented here is related to those interests. All other authors have no competing interests to declare.

FUNDING. This work was supported by grants from the National Institutes of Health (NHLBI U01 HL157989 to B.G.B and I.S.K; NHLBI R01 HL155906 to B.G.B. and I.S.K., T32HL007284 to A.P.C.; R01HL160665 and R01HL162925 to J.J.S.), The Roddenberry Foundation (B.G.B.), the Younger Family Fund (B.G.B.), Additional Ventures Innovation Award (B.G.B), California Institute for Regenerative Medicine (Z.L.G.), Additional Ventures Catalyst to Independence Award (Z.L.G.), American Heart Association (S.K.H.), Startup and seed funding from Indiana University (S.K.H.), Hellman Family Fund (I.S.K.), UCSF Pediatric Heart Center Catalyst Award (I.S.K), Saving tiny Hearts Society (I.S.K.) and UCSF Anesthesia Research Support (I.S.K.).

DATA AND RESOURCE AVAILABILITY. Cell lines are available under a material transfer agreement. All relevant data is available on NCBI GEO (Accession GSE285168 and GSE285169) and details of the code are available at GitHub (apclarkva/kathiriya-rao-2025).

638 **Fig. 1. Features of gene expression and chromatin accessibility for regulatory networks of**
639 **human iPSC-derived atrial cardiomyocytes (CMs) predict TBX5-sensitive atrial CM identity**.
640 Directed differentiations of human induced pluripotent stem cells (iPSCs) to ventricular or atrial
641 cells were assessed by immunostaining of (A-G) ANP or (H-N) MLC2V (****$p<0.0001$ by two-
642 sided Fisher's exact test). Scale bars denote 20 microns (A-F) and 50 microns (H-M). Cells from
643 two experiments of ventricular or atrial differentiations were analyzed; N depicts number of
644 $ACTN2^+$ or $cTNT^+$ cells analyzed per group. (O,P) Normalized local extracellular action potential
645 (LEAP) by cell type. Representative traces are shown, based on LEAPs from 6 ventricular or 6
646 atrial cells from two biological replicates of ventricular or atrial differentiations. (Q) Violin plot of
647 ventricular- or atrial-enriched CM genes. scRNA-seq from two biological replicates of ventricular
648 or atrial differentiations were analyzed. (R) Overlapping chromatin accessible regions. Bar plot
649 shows number of common accessible regions by less than 90% overlap or greater than or equal
650 to 90% overlap. (S) Motifs enriched in differentially accessible regions (DARs) (FDR<0.1).
651 snATAC-seq from two biological replicates of ventricular or atrial differentiations were analyzed
652 in (R, S). Gene regulatory networks (GRNs) of (T) ventricular or (U) atrial CMs. Wheel diagrams
653 for *TBX5* show a shift in significant direct connections between (V) ventricular and (W) atrial CMs.
654 GRNs were derived from two experiments of scRNA-seq or snATAC-seq during ventricular or
655 atrial differentiations. Based on input from the UMAP of atrial CM cell types in (X) wildtype, *in*
656 *silico* prediction by CellOracle infers the states of individual cells from atrial cardiomyotyces (CMs)
657 to CMs expressing extracellular matrix genes (CMEs) from (Y) complete *TBX5* loss (*TBX5*=0).
658
659 **Fig. S1. Gene expression analyses in human iPSC-derived ventricular or atrial CMs.** UMAPs
660 of scRNA-seq annotated by (A) cell types, (B) differentiation to ventricular or atrial cells, or (C)
661 experimental batch. (D,E) UMAP of CM subset by Louvain cell clustering for subtypes defined by
662 their marker genes. scRNA-seq from two biological replicates of ventricular or atrial
663 differentiations were analyzed.
664
665 **Fig. S2. Chromatin accessibility analyses of human iPSC-derived ventricular or atrial CMs.**
666 (A) UMAP of snATAC-seq by inferred cell type from gene score, or by (B) differentiation. UMAPs
667 of gene scores from snATAC-seq for (B') *TNNT2*, (C) *MYL2* (ventricular CM-enriched) or *MYH6*
668 (atrial CM-enriched). UMAP of snATAC-seq subset of $TNNT2^+$-gene $score^+$ cells inferred as CMs
669 (D) by ventricular or atrial differentiation or (E) by Louvain cell clustering. (F) Bar plot of snATAC-
670 seq peak distribution in the genome by cell cluster. (G) Volcano plot of differential accessible

671 regions enriched in ventricular or atrial CMs (FDR<0.1). snATAC-seq of two biological replicates
672 from ventricular or atrial differentiations were analyzed.
673
674 **Fig. S3. Gene regulatory network (GRN) analyses of human iPSC-derived ventricular or**
675 **atrial CMs.** GRNs display connections of top 10 TFs in (A) ventricular or (B) atrial CMs. Bar plots
676 show top 30 TFs ranked by betweenness centrality scores in (C) ventricular CMs or (D) atrial
677 CMs. Bar plots of selected TFs with known roles in ventricular or atrial CMs show (E) betweenness
678 or (F) degree out centrality. Wheel diagrams of *HEY2* (G, H) or *HEY1* (I, J) display direct
679 connections in ventricular or atrial CMs. GRNs were derived from scRNA-seq or snATAC-seq of
680 two biological replicates during ventricular or atrial differentiations.
681
682 **Fig. S4. Analysis of a human cellular model of atrial disease.** (A) Western blot and (B)
683 quantification of TBX5 by *TBX5* genotype (*p<0.05 by two-sided Welch's T-test). Representative
684 Western blot is based on three experiments. (C-E) Example images of atrial CMs by sarcomere
685 disarray scores. (F) UMAP of scRNA-seq at day 20 of atrial differentiation by experimental batch.
686 (G) Bar plot shows cell types at day 20 by *TBX5* genotypes. scRNA-seq of two biological
687 replicates by *TBX5* genotype were analyzed.
688
689 **Fig. 2. Modeling genetic susceptibility to reduced TBX5 in human iPSC-derived atrial cells**
690 **reveals atrial CM dysfunction.** (A) Differentiation efficiency by flow cytometry of cTNT (**p<0.01,
691 ***p<0.001 by two-sided Student's T-test). (B-E) cTNT immunostaining shows sarcomeric
692 disarray in *TBX5* mutant atrial CMs (*p<0.05, ****p<0.0001 by two-sided Fisher's exact test). (F)
693 Average cell area is significantly increased in *TBX5* mutant atrial CMs (*p<0.05, ****p<0.0001 by
694 two-sided Student's T-test). Cells from two biological replicates were analyzed in (E,F). (G, H)
695 Representative action potential traces by MEA, based on cells from two experiments (N=6 in
696 controls, 20 in $TBX5^{in/+}$). (I-J) Field potential and normalized local extracellular action potential
697 durations at 90% (APD_{90}) are increased in *TBX5* heterozygous mutant atrial CMs (****p<0.0001
698 by two-sided Welch's T-test). (K) UMAP displays scRNA-seq data at day 20 by (K) *TBX5* genotype
699 or (L) cell type labels. (M) Dot plot of genes used to define cell types. (N) Distribution of cell types
700 by *TBX5* genotypes shows reduced CMs and increased fibroblasts and epithelial-like cells in
701 $TBX5^{in/del}$ (***adj. p<0.001 by linear regression). $TBX5^{in/+}$ remains largely similar to WT. (O,P) Milo
702 analysis showed a statistically significant difference in the abundance of CMs, fibroblasts,
703 epithelial and neural-like cells for $TBX5^{in/del}$ (FDR<0.05). scRNA-seq of two biological replicates
704 by *TBX5* genotype were analyzed.

705
706
707 **Fig. 3. Atrial CM identity by gene expression is vulnerable to reduced TBX5 dosage.** UMAP
708 of *TNNT2*+ cells colored by (A) genotype, (B) cell type markers or (C) cell type labels. (D)
709 Monocole 3 analysis shows the predominant pseuodtime paths (i.e., in pseudocolor, represented
710 by the arrows) in two partitions affected in *TBX5*$^{in/del}$. Specifically, in partition 2, fewer *TBX5*$^{in/del}$
711 cells reach the end of the pseudotime path to *NPPA*$^{+}$ CMs. (E) Cell numbers of many atrial CM
712 cell types are significantly reduced in *TBX5* mutants. (*adj. p<0.05 **adj. p<0.01, ***adj. p<0.001
713 by linear regression). (F,G) Volcano plots show differentially expressed genes in *TBX5* mutants
714 (adj. p-value by Wilcoxan rank sum). (H) Categories of down- and up-regulated genes in *TBX5*$^{in/+}$
715 or *TBX5*$^{in/\mathrm{del}}$ (adj. p<0.05 by Wilcoxan rank sum). (I-K) AF-, ASD- and CHD-risk genes are
716 enriched among differentially expressed TBX5-sensitive genes (non-adjusted p-value by
717 hypergeometric test). Dot plots of differentially-expressed CHD, ASD (in green) and AF genes in
718 (L) *TBX5*$^{in/+}$ or (M) in both *TBX5*$^{in/+}$ and *TBX5*$^{in/del}$ (adj. p<0.05 by Wilcoxan rank sum). scRNA-seq
719 of two biological replicates by *TBX5* genotype were analyzed.
720
721 **Fig. S5. Analysis of CMs in a human cellular model of atrial disease.** (A) Bar plot shows CM
722 subtypes at day 20 by *TBX5* genotypes. scRNA-seq of two biological replicates by *TBX5* genotype
723 were analyzed.
724
725 **Fig. 4. TBX5-dependent genes are dysregulated in human iPSC-derived atrial cells by**
726 **fluorescent *in situ* hybridization.** Gene expression in WT or *TBX5* mutants of *TNNT2* and
727 *NR2F1* (A-C), *DES* (D-F), fibrosis modulator *ANGPT1* (G-I), and cardiac fibrobast-enriched *MEG3*
728 (J-M) (***p<0.001 by two-sided Fisher's exact test). All scale bars denote 50 microns. Two
729 experiments by *TBX5* genotype were analyzed.
730
731 **Fig. S6. Dysregulated gene expression in human iPSC-derived atrial cells of *TBX5***
732 **heterozygous mutants at day 45 by scRNA-seq**. UMAP by (A) genotype or (B) cell type label
733 at day 45. (C) Feature plots of marker genes for cell type labels. (D) Bar plot shows distribution
734 of cell types in WT or *TBX5*$^{in/+}$, including a reduction in CMs in *TBX5* mutants (*adj. p<0.05, ***adj.
735 p<0.001 by linear regression). UMAP of CM subtypes by (E) genotype or (F) CM subtype labels.
736 (G) Feature plot of marker genes for CM subtype labels. (H) Bar plot shows distribution of CM
737 subtypes in WT or *TBX5*$^{in/+}$, including alterations to several CM subtypes (**adj. p<0.01, ***adj.
738 p<0.001 by linear regression). (I) Volcano plot shows diferentially expressed genes (adj. p-value

739 by Wilcoxan rank sum). (J-L) CHD-, ASD- and AF-risk genes are enriched among differentially
740 expressed TBX5-sensitive genes at day 45 (non-adjusted p-value by hypergeometric test). Dot
741 plots display differentially-expressed CHD, ASD (in green) and AF genes in (M) *TBX5*$^{in/+}$ (adj.
742 p<0.05 by Wilcoxan rank sum). scRNA-seq of two biological replicates by *TBX5* genotype were
743 analyzed.
744
745 **Fig. S7. Comparison of differential gene expression in human iPSC-derived atrial cells of**
746 ***TBX5* heterozygous mutants at day 20 and day 45**. UMAP of CM subtypes in merged data of
747 day 20 and day 45 by (A) *TBX5* genotype and (B) CM subtype labels. (C) Dot plots of differentially-
748 expressed CHD, ASD (highlighted in green) and AF genes in *TBX5*$^{in/+}$ in merged data of day 20
749 and day 45 (adj. p-value<0.05 by Wilcoxan rank sum). scRNA-seq of two biological replicates by
750 *TBX5* genotype at day 20 or day 45 were analyzed.
751
752
753 **Fig. 5. TBX5-sensitive chromatin regions in human iPSC-derived atrial cells show reduced**
754 **accessibility at sites normally bound by TBX5**. UMAP of all atrial cells colored by (A) *TBX5*
755 genotype or (B) *TNNT2*$^{+}$-gene score. UMAP of *TNNT2*$^{+}$-gene score cells colored by (C) *TBX5*
756 genotype or (D) cluster. (E-F) Motifs enriched in differentially accessible regions (DARs) in (E)
757 *TBX5*$^{in/del}$ or (F) *TBX5*$^{in/+}$ (FDR<0.1). DARs with (G) predicted TBX or MEIS motifs or (G') TBX5
758 occupancy by TBX5 ChIP-seq. Browser track shows scATAC peaks near (H) *NPPA-NPPB* or (I)
759 *NR2F1*. Gray shading indicates DARs. TBX5 occupancy in WT cells by TBX5 ChIP-seq (Grant et
760 al. 2024). snATAC-seq of two biological replicates by *TBX5* genotype were analyzed.
761
762
763 **Fig. S8. Analysis of chromatin accessibility in human iPSC-derived atrial cells of *TBX5***
764 **mutants.** (A) Feature plots of gene scores identify putative cell types from chromatin accessibility.
765 (B) Feature plots of gene scores identify putative CM subtypes from chromatin accessibility. (C)
766 Genomic distribution of peaks by cluster. Differentially accessible peaks in (D) *TBX5*$^{in/+}$ or (E)
767 *TBX5*$^{in/del}$. (F-I) Overlap of genes near DARs and differential gene expression in *TBX5* mutants.
768 (J, K) Overlap of DARs in *TBX5*$^{in/+}$ and *TBX5*$^{in/del}$. Two biological replicates of snATAC-seq by
769 *TBX5* genotype were analyzed.
770
771 **Fig. 6. Proper TBX5 dosage controls disease-linked atrial CM gene regulatory networks**
772 **(GRNs).** (A-C) GRNs of atrial CMs with selected TFs by *TBX5* genotype. Grey lines indicate

773 positive correlations. Red lines depict negative correlations. Genes that are edges are unlabeled
774 for simplicity of the diagram. (D-F) Priority networks of atrial CMs shows TF sources to TBX5 or
775 CHD- , ASD- (in green) or AF-risk genes in *TBX5* mutants. (G) Betweenness or (H) degree out
776 centrality of selected TFs in GRNs. Wheel diagrams of (I) *NR2F1* or (J) *TBX5*. Strength of black
777 arrows depicts strength of positive correlation, while strength of red arrows depicts strength of
778 negative correlations. (K) Inverse wheel diagram of *NPPA* shows connections to other TFs that
779 are gained or lost from reduced TBX5 dosage. Two samples of scRNA-seq or snATAC-seq by
780 *TBX5* genotype were analyzed.
781
782 **Fig. S9. Network analysis of *TBX5* mutants in human iPSC-derived atrial CMs.** Venn
783 diagrams show overlap of (A) nodes or (B) edges in the same direction in *TBX5* mutants. Wheel
784 diagrams of (E) ASD- and AF-risk *NKX2-5*, (F) ASD-risk *NR2F2*, (G) fibroblast-associated *TCF21*,
785 and (H) fibroblast-associated *TCF12*. Strength of black arrows depicts strength of positive
786 correlation, while strength of red arrows depicts strength of negative correlations. GRNs were
787 derived from scRNA-seq or snATAC-seq of two biological replicates by *TBX5* genotype.
788
789 **Fig. S10. Altered connections to TBX5-dependent target edges in human iPSC-derived**
790 **atrial CMs of *TBX5* mutants.** Inverse wheel diagrams show connections of (A) *BMP5*, (B) *PNISR*
791 and (C) *PGAM1* to other TFs that are gained or lost from reduced TBX5 dosage. GRNs were
792 derived from scRNA-seq or snATAC-seq of two biological replicates by *TBX5* genotype.
793
794 **Table S1**. Table of differentially expressed genes between an *MYH6*$^+$-enriched cluster of atrial
795 CMs and an *MYL2*$^+$-enriched cluster of ventricular CMs.
796
797 **Table S2**. Table of differentially accessible regions between *MYH6*-gene score$^+$ atrial CM and
798 *MYL2*-gene score$^+$ ventricular CM clusters.
799
800 **Table S3**. Table of sources and targets in networks for atrial CM or ventricular CM clusters.
801
802 **Table S4**. Table of differentially expressed genes among *TNNT2*$^+$ clusters by TBX5 genotype.
803
804 **Table S5**. Lists of disease-risk genes for CHDs, ASDs, AF, and ASDs and AF.
805

806 **Table S6**. Table of differentially accessible regions of *TNNT2*-gene score^{+} CM clusters by *TBX5*
807 genotype.
808
809 **Table S7**. Table of sources and targets in networks for CM clusters from atrial CM differentiation
810 by *TBX5* genotype.
811
812 **Bibliography.**
813

814 **Bartholin, L., Powers, S. E., Melhuish, T. A., Lasse, S., Weinstein, M. and Wotton, D.**
815 (2006). TGIF Inhibits Retinoid Signaling. *Mol. Cell. Biol.* **26**, 990–1001.

816 **Basson, C. T., Cowley, G. S., Solomon, S. D., Weissman, B., Poznanski, A. K., Traill, T. A.,**
817 **Seidman, J. G. and Seidman, C. E.** (1994). The clinical and genetic spectrum of the Holt-
818 Oram syndrome (heart-hand syndrome). *N Engl J Med* **330**, 885–891.

819 **Basson, C. T., Bachinsky, D. R., Lin, R. C., Levi, T., Elkins, J. A., Soults, J., Grayzel, D.,**
820 **Kroumpouzou, E., Traill, T. A., Leblanc-Straceski, J., et al.** (1997). Mutations in human
821 TBX5 [corrected] cause limb and cardiac malformation in Holt-Oram syndrome. *Nat Genet*
822 **15**, 30–35.

823 **Bates, D., Mächler, M., Bolker, B. and Walker, S.** (2015). Fitting Linear Mixed-Effects Models
824 Using lme4. *J. Stat. Softw.* **67**,.

825 **Benjamini, Y. and Hochberg, Y.** (1995). Controlling the False Discovery Rate - a Practical and
826 Powerful Approach to Multiple Testing. *Journal of the Royal Statistical Society Series B-*
827 *Statistical Methodology* **57**, 289–300.

828 **Benson, D. W., Sharkey, A., Fatkin, D., Lang, P., Basson, C. T., McDonough, B., Strauss,**
829 **A. W., Seidman, J. G. and Seidman, C. E.** (1998). Reduced penetrance, variable
830 expressivity, and genetic heterogeneity of familial atrial septal defects. *Circulation* **97**, 2043–
831 2048.

832 **Benson, D. W., Wang, D. W., Dyment, M., Knilans, T. K., Fish, F. A., Strieper, M. J.,**
833 **Rhodes, T. H. and George, A. L.** (2003). Congenital sick sinus syndrome caused by
834 recessive mutations in the cardiac sodium channel gene (SCN5A). *J. Clin. Investig.* **112**,
835 1019–1028.

836 **Bersell, K. R., Yang, T., Mosley, J. D., Glazer, A. M., Hale, A. T., Kryshtal, D. O., Kim, K.,**
837 **Steimle, J. D., Brown, J. D., Salem, J.-E., et al.** (2023). Transcriptional Dysregulation
838 Underlies Both Monogenic Arrhythmia Syndrome and Common Modifiers of Cardiac
839 Repolarization. *Circulation* **147**, 824–840.

840 **Bever, Y. van, Dijkstra, P. F. and Hennekam, R. C. M.** (1996). Autosomal dominant familial
841 radial luxation, carpal fusion and scapular dysplasia with variable heart defects. *Am. J. Méd.*
842 *Genet.* **65**, 213–217.

843 **Boniel, S., Szymańska, K., Śmigiel, R. and Szczałuba, K.** (2021). Kabuki Syndrome—Clinical
844 Review with Molecular Aspects. *Genes-basel* **12**, 468.

845 **Briganti, F., Sun, H., Wei, W., Wu, J., Zhu, C., Liss, M., Karakikes, I., Rego, S., Cipriano, A.,**
846 **Snyder, M., et al.** (2020). iPSC Modeling of RBM20-Deficient DCM Identifies Upregulation of
847 RBM20 as a Therapeutic Strategy. *Cell Rep.* **32**, 108117.

848 **Bruneau, B. G., Nemer, G., Schmitt, J. P., Charron, F., Robitaille, L., Caron, S., Conner, D.**
849 **A., Gessler, M., Nemer, M., Seidman, C. E., et al.** (2001). A Murine Model of Holt-Oram
850 Syndrome Defines Roles of the T-Box Transcription Factor Tbx5 in Cardiogenesis and
851 Disease. *Cell* **106**, 709–721.

852 **Burstein, B., Libby, E., Calderone, A. and Nattel, S.** (2008). Differential Behaviors of Atrial
853 Versus Ventricular Fibroblasts. *Circulation* **117**, 1630–1641.

854 **Bushdid, P. B., Osinska, H., Waclaw, R. R., Molkentin, J. D. and Yutzey, K. E.** (2003).
855 NFATc3 and NFATc4 Are Required for Cardiac Development and Mitochondrial Function.
856 *Circ. Res.* **92**, 1305–1313.

857 **Campione, M., Ros, M. A., Icardo, J. M., Piedra, E., Christoffels, V. M., Schweickert, A.,**
858 **Blum, M., Franco, D. and Moorman, A. F. M.** (2001). Pitx2 Expression Defines a Left
859 Cardiac Lineage of Cells: Evidence for Atrial and Ventricular Molecular Isomerism in the iv/iv
860 Mice. *Dev. Biol.* **231**, 252–264.

861 **Cao, J., Spielmann, M., Qiu, X., Huang, X., Ibrahim, D. M., Hill, A. J., Zhang, F., Mundlos,**
862 **S., Christiansen, L., Steemers, F. J., et al.** (2019). The single-cell transcriptional landscape
863 of mammalian organogenesis. *Nature* **34**, 65–31.

864 **Chen, Y.-H., Xu, S.-J., Bendahhou, S., Wang, X.-L., Wang, Y., Xu, W.-Y., Jin, H.-W., Sun, H.,**
865 **Su, X.-Y., Zhuang, Q.-N., et al.** (2003). KCNQ1 Gain-of-Function Mutation in Familial Atrial
866 Fibrillation. *Science* **299**, 251–254.

867 **Ching, Y.-H., Ghosh, T. K., Cross, S. J., Packham, E. A., Honeyman, L., Loughna, S.,**
868 **Robinson, T. E., Dearlove, A. M., Ribas, G., Bonser, A. J., et al.** (2005). Mutation in
869 myosin heavy chain 6 causes atrial septal defect. *Nat Genet* **37**, 423–428.

870 **Choi, S. H., Weng, L.-C., Roselli, C., Lin, H., Haggerty, C. M., Shoemaker, M. B., Barnard,**
871 **J., Arking, D. E., Chasman, D. I., Albert, C. M., et al.** (2018). Association Between Titin
872 Loss-of-Function Variants and Early-Onset Atrial Fibrillation. *Jama* **320**, 2354.

873 **Cyganek, L., Tiburcy, M., Sekeres, K., Gerstenberg, K., Bohnenberger, H., Lenz, C.,**
874 **Henze, S., Stauske, M., Salinas, G., Zimmermann, W.-H., et al.** (2018). Deep phenotyping
875 of human induced pluripotent stem cell–derived atrial and ventricular cardiomyocytes. *JCI*
876 *Insight* **3**, 1–18.

877 **Dai, W., Laforest, B., Tyan, L., Shen, K. M., Nadadur, R. D., Alvarado, F. J., Mazurek, S. R.,**
878 **Lazarevic, S., Gadek, M., Wang, Y., et al.** (2019). A calcium transport mechanism for atrial
879 fibrillation in Tbx5-mutant mice. *eLife* **8**, 40.

880 **Dann, E., Henderson, N. C., Teichmann, S. A., Morgan, M. D. and Marioni, J. C.** (2022).
881 Differential abundance testing on single-cell data using k-nearest neighbor graphs. *Nat.*
882 *Biotechnol.* **40**, 245–253.

883 **DeLaughter, D. M., Bick, A. G., Wakimoto, H., McKean, D., Gorham, J. M., Kathiriya, I. S.,**
884 **Hinson, J. T., Homsy, J., Gray, J., Pu, W., et al.** (2016). Single-Cell Resolution of Temporal
885 Gene Expression during Heart Development. *Dev Cell* **39**, 1–25.

886 **Desjardins, C. and Naya, F.** (2016). The Function of the MEF2 Family of Transcription Factors
887 in Cardiac Development, Cardiogenomics, and Direct Reprogramming. *JCDD* **3**, 26–19.

888 **Devalla, H. D., Schwach, V., Ford, J. W., Milnes, J. T., Haou, S. E., Jackson, C., Gkatzis, K.,**
889 **Elliott, D. A., Lopes, S. M. C. de S., Mummery, C. L., et al.** (2015). Atrial-like
890 cardiomyocytes from human pluripotent stem cells are a robust preclinical model for
891 assessing atrial-selective pharmacology. *EMBO Mol Med* **7**, 394–410.

892 **Devalla, H. D., Gélinas, R., Aburawi, E. H., Beqqali, A., Goyette, P., Freund, C., Chaix, M.**
893 **A., Tadros, R., Jiang, H., Béchec, A. L., et al.** (2016). TECRL, a new life-threatening
894 inherited arrhythmia gene associated with overlapping clinical features of both LQTS and
895 CPVT. *EMBO Mol Med* **8**, 1390–1408.

896 **Dobrev, D., Aguilar, M., Heijman, J., Guichard, J.-B. and Nattel, S.** (2019). Postoperative
897 atrial fibrillation: mechanisms, manifestations and management. *Nat Rev Cardiol* **16**, 1–20.

898 **Friedman, C. E., Fayer, S., Pendyala, S., Chien, W.-M., Loiben, A., Tran, L., Chao, L. S.,**
899 **McKinstry, A., Ahmed, D., Farris, S. D., et al.** (2024). Multiplexed Functional Assessments
900 of MYH7 Variants in Human Cardiomyocytes. *Circ.: Genom. Precis. Med.* **17**, e004377.

901 **Garg, V., Kathiriya, I. S., Barnes, R., Schluterman, M. K., King, I. N., Butler, C. A.,**
902 **Rothrock, C. R., Eapen, R. S., Hirayama-Yamada, K., Joo, K., et al.** (2003). GATA4
903 mutations cause human congenital heart defects and reveal an interaction with TBX5. *Nature*
904 **424**, 443–447.

905 **Garg, V., Muth, A. N., Ransom, J. F., Schluterman, M. K., Barnes, R., King, I. N., Grossfeld,**
906 **P. D. and Srivastava, D.** (2005). Mutations in NOTCH1 cause aortic valve disease. *Nature*
907 **437**, 270–274.

908 **Gise, A. von, Lin, Z., Schlegelmilch, K., Honor, L. B., Pan, G. M., Buck, J. N., Ma, Q.,**
909 **Ishiwata, T., Zhou, B., Camargo, F. D., et al.** (2012). YAP1, the nuclear target of Hippo
910 signaling, stimulates heart growth through cardiomyocyte proliferation but not hypertrophy.
911 *Proc. Natl. Acad. Sci.* **109**, 2394–2399.

912 **Goldfracht, I., Protze, S., Shiti, A., Setter, N., Gruber, A., Shaheen, N., Nartiss, Y., Keller,**
913 **G. and Gepstein, L.** (2019). Generating ring-shaped engineered heart tissues from
914 ventricular and atrial human pluripotent stem cell-derived cardiomyocytes. *Nat Commun* 1–
915 15.

916 **Granja, J. M., Corces, M. R., Pierce, S. E., Bagdatli, S. T., Choudhry, H., Chang, H. Y. and**
917 **Greenleaf, W. J.** (2020). ArchR: An integrative and scalable software package for single-cell
918 chromatin accessibility analysis. **37**, 916–86.

Granja, J. M., Corces, M. R., Pierce, S. E., Bagdatli, S. T., Choudhry, H., Chang, H. Y. and Greenleaf, W. J. (2021). ArchR is a scalable software package for integrative single-cell chromatin accessibility analysis. *Nat Genet* **53**, 403–411.

Grant, Z. L., Kuang, S., Zhang, S., Horrillo, A. J., Rao, K. S., Kameswaran, V., Joubran, C., Lau, P. K., Dong, K., Yang, B., et al. (2025). Dose-dependent sensitivity of human 3D chromatin to a heart disease-linked transcription factor. *bioRxiv* 2025.01.09.632202.

Gudbjartsson, D. F., Holm, H., Sulem, P., Masson, G., Oddsson, A., Magnusson, O. Th., Saemundsdottir, J., Helgadottir, H. Th., Helgason, H., Johannsdottir, H., et al. (2016). A frameshift deletion in the sarcomere gene MYL4 causes early-onset familial atrial fibrillation. *Eur Heart J* **38**, 27–34.

Guo, D.-F., Li, R.-G., Yuan, F., Shi, H.-Y., Hou, X.-M., Qu, X.-K., Xu, Y.-J., ZHANG, M., LIU, X., JIANG, J.-Q., et al. (2016). TBX5 loss-of-function mutation contributes to atrial fibrillation and atypical Holt-Oram syndrome. *Mol Med Rep* **13**, 4349–4356.

Hagberg, A. A., Schult, D. A. and Swart, P. J. (2008). Exploring Network Structure, Dynamics, and Function using NetworkX. *Proc. 7th Python Sci. Conf.* 11–15.

Hao, Y., Hao, S., Andersen-Nissen, E., Mauck, W. M., Zheng, S., Butler, A., Lee, M. J., Wilk, A. J., Darby, C., Zager, M., et al. (2021). Integrated analysis of multimodal single-cell data. *Cell* **184**, 3573-3587.e29.

Hinson, J. T., Chopra, A., Nafissi, N., Polacheck, W. J., Benson, C. C., Swist, S., Gorham, J., Yang, L., Schafer, S., Sheng, C. C., et al. (2015). HEART DISEASE. Titin mutations in iPS cells define sarcomere insufficiency as a cause of dilated cardiomyopathy. *Science* **349**, 982–986.

Hnatiuk, A. P., Briganti, F., Staudt, D. W. and Mercola, M. (2021). Human iPSC modeling of heart disease for drug development. *Cell Chem. Biol.* **28**, 271–282.

Hodgson-Zingman, D. M., Karst, M. L., Zingman, L. V., Heublein, D. M., Darbar, D., Herron, K. J., Ballew, J. D., Andrade, M. de, Burnett, J. C. and Olson, T. M. (2008). Atrial Natriuretic Peptide Frameshift Mutation in Familial Atrial Fibrillation. *New Engl J Medicine* **359**, 158–165.

Hoffman, J. I. E. and Kaplan, S. (2002). The incidence of congenital heart disease. *J Am Coll Cardiol* **39**, 1890–1900.

Hong, K., Bjerregaard, P., Gussak, I. and Brugada, R. (2005). Short QT Syndrome and Atrial Fibrillation Caused by Mutation in KCNH2. *J Cardiovasc Electr* **16**, 394–396.

Horsthuis, T., Houweling, A. C., Habets, P. E. M. H., Lange, F. J. D., Azzouzi, H. el, Clout, D. E. W., Moorman, A. F. M. and Christoffels, V. M. (2008). Distinct Regulation of Developmental and Heart Disease-Induced Atrial Natriuretic Factor Expression by Two Separate Distal Sequences. *Circ Res* **102**, 849–859.

955 **Kamimoto, K., Stringa, B., Hoffmann, C. M., Jindal, K., Solnica-Krezel, L. and Morris, S. A.**
956 (2023). Dissecting cell identity via network inference and in silico gene perturbation. *Nature*
957 **614**, 742–751.

958 **Karakikes, I., Termglinchan, V., Cepeda, D. A., Lee, J., Diecke, S., Hendel, A., Itzhaki, I.,**
959 **Ameen, M., Shrestha, R., Wu, H., et al.** (2017). A Comprehensive TALEN-Based Knockout
960 Library for Generating Human-Induced Pluripotent Stem Cell-Based Models for
961 Cardiovascular Diseases. *Circ Res* **120**, 1561–1571.

962 **Kathiriya, I. S., Rao, K. S., Iacono, G., Devine, W. P., Blair, A. P., Hota, S. K., Lai, M. H.,**
963 **Garay, B. I., Thomas, R., Gong, H. Z., et al.** (2021). Modeling Human TBX5
964 Haploinsufficiency Predicts Regulatory Networks for Congenital Heart Disease. *Dev Cell* **56**,
965 292-309.e9.

966 **Kim, K. H., Nakaoka, Y., Augustin, H. G. and Koh, G. Y.** (2018). Myocardial Angiopoietin-1
967 Controls Atrial Chamber Morphogenesis by Spatiotemporal Degradation of Cardiac Jelly.
968 *Cell Rep.* **23**, 2455–2466.

969 **King, I. N., Qian, L., Liang, J., Huang, Y., Shieh, J. T. C., Kwon, C. and Srivastava, D.**
970 (2011). A genome-wide screen reveals a role for microRNA-1 in modulating cardiac cell
971 polarity. *Dev Cell* **20**, 497–510.

972 **Kirk, E. P., Sunde, M., Costa, M. W., Rankin, S. A., Wolstein, O., Castro, M. L., Butler, T. L.,**
973 **Hyun, C., Guo, G., Otway, R., et al.** (2007). Mutations in cardiac T-box factor gene TBX20
974 are associated with diverse cardiac pathologies, including defects of septation and
975 valvulogenesis and cardiomyopathy. *Am J Hum Genet* **81**, 280–291.

976 **Kitamura, K., Miura, H., Miyagawa-Tomita, S., Yanazawa, M., Katoh-Fukui, Y., Suzuki, R.,**
977 **Ohuchi, H., Suehiro, A., Motegi, Y., Nakahara, Y., et al.** (1999). Mouse Pitx2 deficiency
978 leads to anomalies of the ventral body wall, heart, extra- and periocular mesoderm and right
979 pulmonary isomerism. *Development* **126**, 5749–5758.

980 **Knollmann, B. C.** (2013). Induced Pluripotent Stem Cell–Derived Cardiomyocytes. *Circ. Res.*
981 **112**, 969–976.

982 **Kornej, J., Börschel, C. S., Benjamin, E. J. and Schnabel, R. B.** (2020). Epidemiology of
983 Atrial Fibrillation in the 21st Century. *Circ. Res.* **127**, 4–20.

984 **Lan, F., Lee, A. S., Liang, P., Sanchez-Freire, V., Nguyen, P. K., Wang, L., Han, L., Yen, M.,**
985 **Wang, Y., Sun, N., et al.** (2013). Abnormal Calcium Handling Properties Underlie Familial
986 Hypertrophic Cardiomyopathy Pathology in Patient-Specific Induced Pluripotent Stem Cells.
987 *Cell Stem Cell* **12**, 101–113.

988 **Lee, J. H., Protze, S. I., Laksman, Z., Backx, P. H. and Keller, G. M.** (2017). Human
989 Pluripotent Stem Cell-Derived Atrial and Ventricular Cardiomyocytes Develop from Distinct
990 Mesoderm Populations. *Cell Stem Cell* **21**, 179-194.e4.

991 **Lee, S.-P., Ashley, E. A., Homburger, J., Caleshu, C., Green, E. M., Jacoby, D., Colan, S.**
992 **D., Arteaga-Fernández, E., Day, S. M., Girolami, F., et al.** (2018). Incident Atrial Fibrillation

993 Is Associated With MYH7 Sarcomeric Gene Variation in Hypertrophic Cardiomyopathy.
994 *Circulation Hear Fail* **11**, e005191.

995 **Li, Q. Y., Newbury-Ecob, R. A., Terrett, J. A., Wilson, D. I., Curtis, A. R., Yi, C. H., Gebuhr,**
996 **T., Bullen, P. J., Robson, S. C., Strachan, T., et al.** (1997). Holt-Oram syndrome is caused
997 by mutations in TBX5, a member of the Brachyury (T) gene family. *Nat Genet* **15**, 21–29.

998 **Lin, Z., Guo, H., Cao, Y., Zohrabian, S., Zhou, P., Ma, Q., VanDusen, N., Guo, Y., Zhang, J.,**
999 **Stevens, S. M., et al.** (2016). Acetylation of VGLL4 Regulates Hippo-YAP Signaling and
1000 Postnatal Cardiac Growth. *Dev. Cell* **39**, 466–479.

1001 **Litviňuková, M., Talavera-López, C., Maatz, H., Reichart, D., Worth, C. L., Lindberg, E. L.,**
1002 **Kanda, M., Polanski, K., Heinig, M., Lee, M., et al.** (2020). Cells of the adult human heart.
1003 *Nature* **588**, 466–472.

1004 **Liu, C., Liu, W., Palie, J., Lu, M. F., Brown, N. A. and Martin, J. F.** (2002). Pitx2c patterns
1005 anterior myocardium and aortic arch vessels and is required for local cell movement into
1006 atrioventricular cushions. *Development* **129**, 5081–5091.

1007 **Liu, N., Schoch, K., Luo, X., Pena, L. D. M., Bhavana, V. H., Kukolich, M. K., Stringer, S.,**
1008 **Powis, Z., Radtke, K., Mroske, C., et al.** (2018). Functional variants in TBX2 are associated
1009 with a syndromic cardiovascular and skeletal developmental disorder. *Hum. Mol. Genet.* **27**,
1010 2454–2465.

1011 **Luna-Zurita, L., Stirnimann, C. U., Glatt, S., Kaynak, B. L., Thomas, S., Baudin, F., Samee,**
1012 **M. A. H., He, D., Small, E. M., Mileikovsky, M., et al.** (2016). Complex Interdependence
1013 Regulates Heterotypic Transcription Factor Distribution and Coordinates Cardiogenesis. *Cell*
1014 **164**, 999–1014.

1015 **Ma, J.-F., Yang, F., Mahida, S. N., Zhao, L., Chen, X., Zhang, M. L., Sun, Z., Yao, Y., Zhang,**
1016 **Y.-X., Zheng, G.-Y., et al.** (2016). TBX5 mutations contribute to early-onset atrial fibrillation
1017 in Chinese and Caucasians. *Cardiovasc Res* **109**, 442–450.

1018 **Man, J. C. K., Duijvenboden, K. van, Krijger, P. H. L., Hooijkaas, I. B., Made, I. van der,**
1019 **Vries, C. D. G.-D., Wakker, V., Creemers, E. E., Laat, W. de, Boukens, B. J., et al.** (2021).
1020 Genetic Dissection of a Super Enhancer Controlling the Nppa-NppbCluster in the Heart. *Circ*
1021 *Res* **128**, 115–129.

1022 **Matsson, H., Eason, J., Bookwalter, C. S., Klar, J., Gustavsson, P., Sunnegårdh, J., Enell,**
1023 **H., Jonzon, A., Vikkula, M., Gutierrez, I., et al.** (2008). Alpha-cardiac actin mutations
1024 produce atrial septal defects. *Hum. Mol. Genet.* **17**, 256–265.

1025 **McElhinney, D. B., Krantz, I. D., Bason, L., Piccoli, D. A., Emerick, K. M., Spinner, N. B.**
1026 **and Goldmuntz, E.** (2002). Analysis of Cardiovascular Phenotype and Genotype-Phenotype
1027 Correlation in Individuals With a JAG1 Mutation and/or Alagille Syndrome. *Circulation* **106**,
1028 2567–2574.

1029 **Medrano, J. L. and Naya, F. J.** (2017). The transcription factor MEF2A fine-tunes gene
1030 expression in the atrial and ventricular chambers of the adult heart. *J Biol Chem* **292**, 20975–
1031 20988.

1032 **Miguel, I. M. de and Ávila, P.** (2021). Atrial Fibrillation in Congenital Heart Disease. *European*
1033 *Cardiol Rev* **16**, e06.

1034 **Mir, M. B., Charlebois, E., Tsyplenkova, S., Fillebeen, C. and Pantopoulos, K.** (2023).
1035 Cardiac Hamp mRNA Is Predominantly Expressed in the Right Atrium and Does Not
1036 Respond to Iron. *Int. J. Mol. Sci.* **24**, 5163.

1037 **Miyaoka, Y., Chan, A. H., Judge, L. M., Yoo, J., Huang, M., Nguyen, T. D., Lizarraga, P. P.,**
1038 **So, P.-L. and Conklin, B. R.** (2014). Isolation of single-base genome-edited human iPS
1039 cells without antibiotic selection. *Nat Meth* **11**, 291–293.

1040 **Nadadur, R. D., Broman, M. T., Boukens, B., Mazurek, S. R., Yang, X., Boogaard, M. van**
1041 **den, Bekeny, J., Gadek, M., Ward, T., Zhang, M., et al.** (2016). Pitx2 modulates a Tbx5-
1042 dependent gene regulatory network to maintain atrial rhythm. *Science Translational Medicine*
1043 **8**, 354ra115-354ra115.

1044 **Nadeau, M., Georges, R. O., Laforest, B., Yamak, A., Lefebvre, C., Beauregard, J., Paradis,**
1045 **P., Bruneau, B. G., Andelfinger, G. and Nemer, M.** (2010). An endocardial pathway
1046 involving Tbx5, Gata4, and Nos3 required for atrial septum formation. *Proceedings of the*
1047 *National Academy of Sciences* **107**, 19356–19361.

1048 **Nakashima, H., Tsujimura, K., Irie, K., Ishizu, M., Pan, M., Kameda, T. and Nakashima, K.**
1049 (2018). Canonical TGF-β Signaling Negatively Regulates Neuronal Morphogenesis through
1050 TGIF/Smad Complex-Mediated CRMP2 Suppression. *J Neurosci* **38**, 4791–4810.

1051 **Nandi, S. S., Katsurada, K., Mahata, S. K. and Patel, K. P.** (2021). Neurogenic Hypertension
1052 Mediated Mitochondrial Abnormality Leads to Cardiomyopathy: Contribution of UPRmt and
1053 Norepinephrine-miR- 18a-5p-HIF-1α Axis. *Front Physiol* **12**, 718982.

1054 **Naya, F. J., Black, B. L., Wu, H., Bassel-Duby, R., Richardson, J. A., Hill, J. A. and Olson,**
1055 **E. N.** (2002). Mitochondrial deficiency and cardiac sudden death in mice lacking the MEF2A
1056 transcription factor. *Nat. Med.* **8**, 1303–1309.

1057 **Nerbonne, J. M. and Kass, R. S.** (2005). Molecular Physiology of Cardiac Repolarization.
1058 *Physiol. Rev.* **85**, 1205–1253.

1059 **Olson, T. M., Alekseev, A. E., Liu, X. K., Park, S., Zingman, L. V., Bienengraeber, M.,**
1060 **Sattiraju, S., Ballew, J. D., Jahangir, A. and Terzic, A.** (2006). Kv1.5 channelopathy due to
1061 KCNA5 loss-of-function mutation causes human atrial fibrillation. *Hum Mol Genet* **15**, 2185–
1062 2191.

1063 **Ouwerkerk, A. F., Bosada, F. M., Duijvenboden, K., Hill, M. C., Montefiori, L. E., Scholman,**
1064 **K. T., Liu, J., Vries, A. A. F., Boukens, B. J., Ellinor, P. T., et al.** (2019). Identification of
1065 atrial fibrillation associated genes and functional non-coding variants. *Nat Commun* **10**, 1–14.

1066 **Ouwerkerk, A. F. van, Bosada, F. M., Liu, J., Zhang, J., Duijvenboden, K. van, Chaffin, M.,**
1067 **Tucker, N. R., Pijnappels, D., Ellinor, P. T., Barnett, P., et al.** (2020). Identification of
1068 Functional Variant Enhancers Associated With Atrial Fibrillation. *Circ. Res.* **127**, 229–243.

1069 **Ouwerkerk, A. F. van, Bosada, F. M., Duijvenboden, K. van, Houweling, A. C., Scholman,**
1070 **K. T., Wakker, V., Allaart, C. P., Uhm, J.-S., Mathijssen, I. B., Baartscheer, T., et al.**
1071 (2021). Patient-specific TBX5-G125R Variant Induces Profound Transcriptional Deregulation
1072 and Atrial Dysfunction. *Circulation* **145**, 606–619.

1073 **Perrone, G., Unpingco, J. and Lu, H.** (2020). Network visualizations with Pyvis and VisJS.
1074 *arXiv*.

1075 **Piccoli, M.-T., Gupta, S. K., Viereck, J., Foinquinos, A., Samolovac, S., Kramer, F. L., Garg,**
1076 **A., Remke, J., Zimmer, K., Batkai, S., et al.** (2017). Inhibition of the Cardiac Fibroblast–
1077 Enriched lncRNA Meg3 Prevents Cardiac Fibrosis and Diastolic Dysfunction. *Circ. Res.* **121**,
1078 575–583.

1079 **Platonov, P. G.** (2017). Atrial fibrosis: an obligatory component of arrhythmia mechanisms in
1080 atrial fibrillation? *J. Geriatr. Cardiol. : JGC* **14**, 233–237.

1081 **Posch, M. G., Gramlich, M., Sunde, M., Schmitt, K. R., Lee, S. H. Y., Richter, S., Kersten,**
1082 **A., Perrot, A., Panek, A. N., Khatib, I. H. A., et al.** (2010). A gain-of-function TBX20
1083 mutation causes congenital atrial septal defects, patent foramen ovale and cardiac valve
1084 defects. *J Med Genet* **47**, 230–235.

1085 **Postma, A. V., Meerakker, J. B. A. van de, Mathijssen, I. B., Barnett, P., Christoffels, V. M.,**
1086 **Ilgun, A., Lam, J., Wilde, A. A. M., Deprez, R. H. L. and Moorman, A. F. M.** (2008). A gain-
1087 of-function TBX5 mutation is associated with atypical Holt-Oram syndrome and paroxysmal
1088 atrial fibrillation. *Circ Res* **102**, 1433–1442.

1089 **Postma, A. V., Engelen, K. van, Meerakker, J. van de, Rahman, T., Probst, S., Baars, M. J.**
1090 **H., Bauer, U., Pickardt, T., Sperling, S. R., Berger, F., et al.** (2011). Mutations in the
1091 Sarcomere Gene MYH7 in Ebstein Anomaly. *Circ.: Cardiovasc. Genet.* **4**, 43–50.

1092 **Prapa, M., Lago-Docampo, M., Swietlik, E. M., Montani, D., Eyries, M., Humbert, M., Welch,**
1093 **C. L., Chung, W. K., Berger, R. M. F., Bogaard, H. J., et al.** (2022). First Genotype–
1094 Phenotype Study in TBX4 Syndrome: Gain-of-Function Mutations Causative for Lung
1095 Disease. *Am. J. Respir. Crit. Care Med.* **206**, 1522–1533.

1096 **Roselli, C., Chaffin, M. D., Weng, L.-C., Aeschbacher, S., Ahlberg, G., Albert, C. M.,**
1097 **Almgren, P., Alonso, A., Anderson, C. D., Aragam, K. G., et al.** (2018). Multi-ethnic
1098 genome-wide association study for atrial fibrillation. *Nat Genet* 1–15.

1099 **Schott, J. J., Benson, D. W., Basson, C. T., Pease, W., Silberbach, G. M., Moak, J. P.,**
1100 **Maron, B. J., Seidman, C. E. and Seidman, J. G.** (1998). Congenital heart disease caused
1101 by mutations in the transcription factor NKX2-5. *Science* **281**, 108–111.

1102 **Schweickert, A., Campione, M., Steinbeisser, H. and Blum, M.** (2000). Pitx2 isoforms:
1103 involvement of Pitx2c but not Pitx2a or Pitx2b in vertebrate left–right asymmetry. *Mech. Dev.*
1104 **90**, 41–51.

1105 **Seeger, T., Shrestha, R., Lam, C. K., Chen, C., McKeithan, W. L., Lau, E., Wnorowski, A.,**
1106 **McMullen, G., Greenhaw, M., Lee, J., et al.** (2019). A Premature Termination Codon

Mutation in MYBPC3 Causes Hypertrophic Cardiomyopathy via Chronic Activation of Nonsense-Mediated Decay. *Circulation* **139**, 799–811.

Shafaattalab, S., Lin, E., Christidi, E., Huang, H., Nartiss, Y., Garcia, A., Lee, J., Protze, S., Keller, G., Brunham, L., et al. (2019). Ibrutinib Displays Atrial-Specific Toxicity in Human Stem Cell-Derived Cardiomyocytes. *Stem Cell Rep* **12**, 996–1006.

Sinnecker, D., Goedel, A., Laugwitz, K.-L. and Moretti, A. (2013). Induced Pluripotent Stem Cell-Derived Cardiomyocytes. *Circ. Res.* **112**, 961–968.

Smith, J. G. W., Owen, T., Bhagwan, J. R., Mosqueira, D., Scott, E., Mannhardt, I., Patel, A., Barriales-Villa, R., Monserrat, L., Hansen, A., et al. (2018). Isogenic Pairs of hiPSC-CMs with Hypertrophic Cardiomyopathy/LVNC-Associated ACTC1 E99K Mutation Unveil Differential Functional Deficits. *Stem Cell Rep.* **11**, 1226–1243.

Sun, N., Yazawa, M., Liu, J., Han, L., Sanchez-Freire, V., Abilez, O. J., Navarrete, E. G., Hu, S., Wang, L., Lee, A., et al. (2012). Patient-Specific Induced Pluripotent Stem Cells as a Model for Familial Dilated Cardiomyopathy. *Science Translational Medicine* **4**, 130ra47-130ra47.

Sweat, M. E., Cao, Y., Zhang, X., Burnicka-Turek, O., Perez-Cervantes, C., Kulandaisamy, A., Lu, F., Keating, E. M., Akerberg, B. N., Ma, Q., et al. (2023). Tbx5 maintains atrial identity in postnatal cardiomyocytes by regulating an atrial-specific enhancer network. *Nat. Cardiovasc. Res.* **2**, 881–898.

Theodoris, C. V., Zhou, P., Liu, L., Zhang, Y., Nishino, T., Huang, Y., Kostina, A., Ranade, S. S., Gifford, C. A., Uspenskiy, V., et al. (2020). Network-based screen in iPSC-derived cells reveals therapeutic candidate for heart valve disease. *Science* **371**, eabd0724-14.

Turki, S. A., Manickaraj, A. K., Mercer, C. L., Gerety, S. S., Hitz, M.-P., Lindsay, S., D'Alessandro, L. C. A., Swaminathan, G. J., Bentham, J., Arndt, A.-K., et al. (2014). Rare Variants in NR2F2 Cause Congenital Heart Defects in Humans. *Am. J. Hum. Genet.* **94**, 574–585.

Vad, O. B., Paludan-Muller, C., Ahlberg, G., Andreasen, L., Refsgaard, L., Lundegaard, P. R., Haunso, S., Svendsen, J. H. and Olesen, M. S. (2020). Rare coding variants in MYH6 are associated with atrial fibrillation: results from 45,596 exomes representing the general population. *Eur. Hear. J.* **41**, ehaa946.0342.

Xia, M., Jin, Q., Bendahhou, S., He, Y., Larroque, M.-M., Chen, Y., Zhou, Q., Yang, Y., Liu, Y., Liu, B., et al. (2005). A Kir2.1 gain-of-function mutation underlies familial atrial fibrillation. *Biochem Bioph Res Co* **332**, 1012–1019.

Xie, L., Hoffmann, A. D., Burnicka-Turek, O., Friedland-Little, J. M., Zhang, K. and Moskowitz, I. P. (2012). Tbx5-Hedgehog Molecular Networks Are Essential in the Second Heart Field for Atrial Septation. *Dev Cell* **23**, 280–291.

Xie, W.-H., Chang, C., Xu, Y.-J., Li, R.-G., Qu, X.-K., Fang, W.-Y., Liu, X. and Yang, Y.-Q. (2013). Prevalence and spectrum of Nkx2.5 mutations associated with idiopathic atrial fibrillation. *Clinics* **68**, 777–784.

1146 **Yang, Y., Xia, M., Jin, Q., Bendahhou, S., Shi, J., Chen, Y., Liang, B., Lin, J., Liu, Y., Liu,**
1147 **B., et al.** (2004). Identification of a KCNE2 Gain-of-Function Mutation in Patients with
1148 Familial Atrial Fibrillation. *Am J Hum Genetics* **75**, 899–905.

1149 **Yang, X. H., Nadadur, R. D., Hilvering, C. R., Bianchi, V., Werner, M., Mazurek, S. R.,**
1150 **Gadek, M., Shen, K. M., Goldman, J. A., Tyan, L., et al.** (2017). Transcription-factor-
1151 dependent enhancer transcription defines a gene regulatory network for cardiac rhythm.
1152 *eLife* **6**, 1765.

1153 **Yang, D., Gomez-Garcia, J., Funakoshi, S., Tran, T., Fernandes, I., Bader, G. D., Laflamme,**
1154 **M. A. and Keller, G. M.** (2022a). Modeling human multi-lineage heart field development with
1155 pluripotent stem cells. *Cell Stem Cell* **29**, 1382-1401.e8.

1156 **Yang, A., Alankarage, D., Cuny, H., Ip, E. K. K., Almog, M., Lu, J., Das, D., Enriquez, A.,**
1157 **Szot, J. O., Humphreys, D. T., et al.** (2022b). CHDgene: A Curated Database for
1158 Congenital Heart Disease Genes. *Circ.: Genom. Precis. Med.* **15**, e003539.

1159 **Yuan, F., Zhao, L., Wang, J., Zhang, W., Li, X., Qiu, X.-B., Li, R.-G., Xu, Y.-J., Xu, L., Qu, X.-**
1160 **K., et al.** (2013). PITX2c Loss-of-Function Mutations Responsible for Congenital Atrial Septal
1161 Defects. *Int. J. Méd. Sci.* **10**, 1422–1429.

1162 **Zhang, J. Z., Termglinchan, V., Shao, N.-Y., Itzhaki, I., Liu, C., Ma, N., Tian, L., Wang, V. Y.,**
1163 **Chang, A. C. Y., Guo, H., et al.** (2019). A Human iPSC Double-Reporter System Enables
1164 Purification of Cardiac Lineage Subpopulations with Distinct Function and Drug Response
1165 Profiles. *Cell Stem Cell* **24**, 802-811.e5.

1166

1167

Figure 1

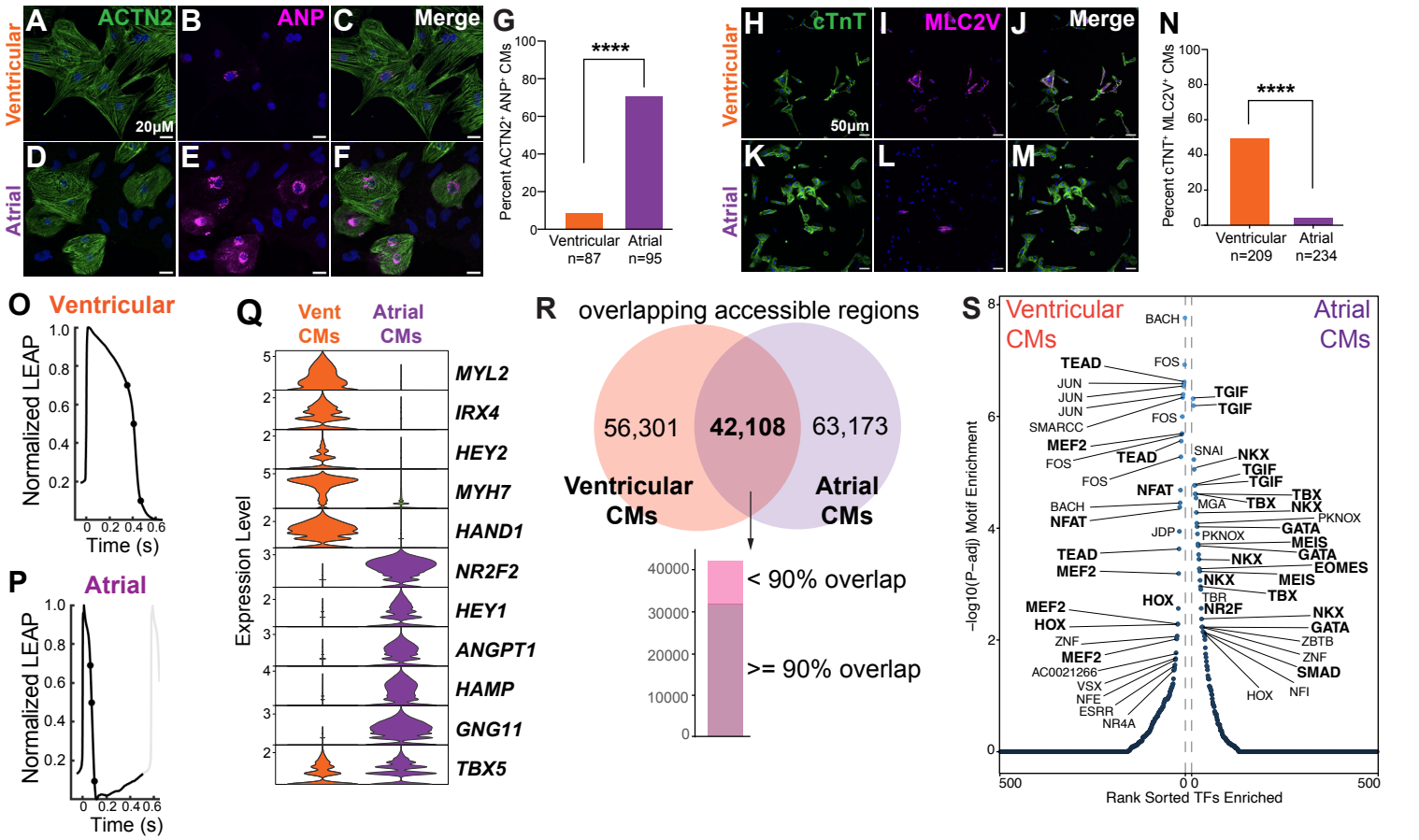
A ACTN2
B ANP
C Merge
Ventricular
Atrial
20μM
D
E
F
G
Percent ACTN2+ ANP+ CMs
****
Ventricular n=87
Atrial n=95
H cTnT
I MLC2V
J Merge
50μm
K
L
M
N
Percent cTNT+ MLC2V+ CMs
Ventricular n=209
Atrial n=234
O Ventricular
Normalized LEAP
Time (s)
P Atrial
Q Vent CMs
Atrial CMs
Expression Level
MYL2
IRX4
HEY2
MYH7
HAND1
NR2F2
HEY1
ANGPT1
HAMP
GNG11
TBX5
R overlapping accessible regions
56,301
42,108
63,173
Ventricular CMs
Atrial CMs
< 90% overlap
>= 90% overlap
S Ventricular CMs
Atrial CMs
−log10(P−adj) Motif Enrichment
Rank Sorted TFs Enriched
BACH
TEAD
FOS
JUN
SMARCC
MEF2
TGIF
SNAI
NKX
NFAT
MGA
TBX
PKNOX
GATA
MEIS
JDP
EOMES
TBR
NR2F
HOX
ZNF
ZBTB
SMAD
AC0021266
VSX
NFE
ESRR
NR4A
NFI
T Ventricular CMs
GATA4
HEY2
NKX2-5
HEY1
TBX5
E2F1
MEF2C
IRX4
HES4
HAND1
MEIS2
V Ventricular CMs
ATP5MG
BMP5
NPPA
RBIS
CAPN3
KIFAP3
SLC8A1
TMED10
PGAM1
SF3B1
PPIC
PNISR
PAM
TBX5
KDELR1
SELENOW
PSMB7
ATP5MD
CNBP
SORBS2
GNG5
CHCHD10
SKP1
PPIA
TXN
CYBA
X CMEs
WT atrial differentiation
Atrial CMs
AV CMs
Vent-like CMs
U Atrial CMs
NKX2-5
NR2F1
HEY2
TBX5
HEY1
NR2F2
HES4
PLAGL1
IRX4
MEF2C
MEIS2
HAND1
W Atrial CMs
Y CMEs
predicted TBX5 loss
Atrial CMs
AV CMs
Vent-like CMs

Fig. S1

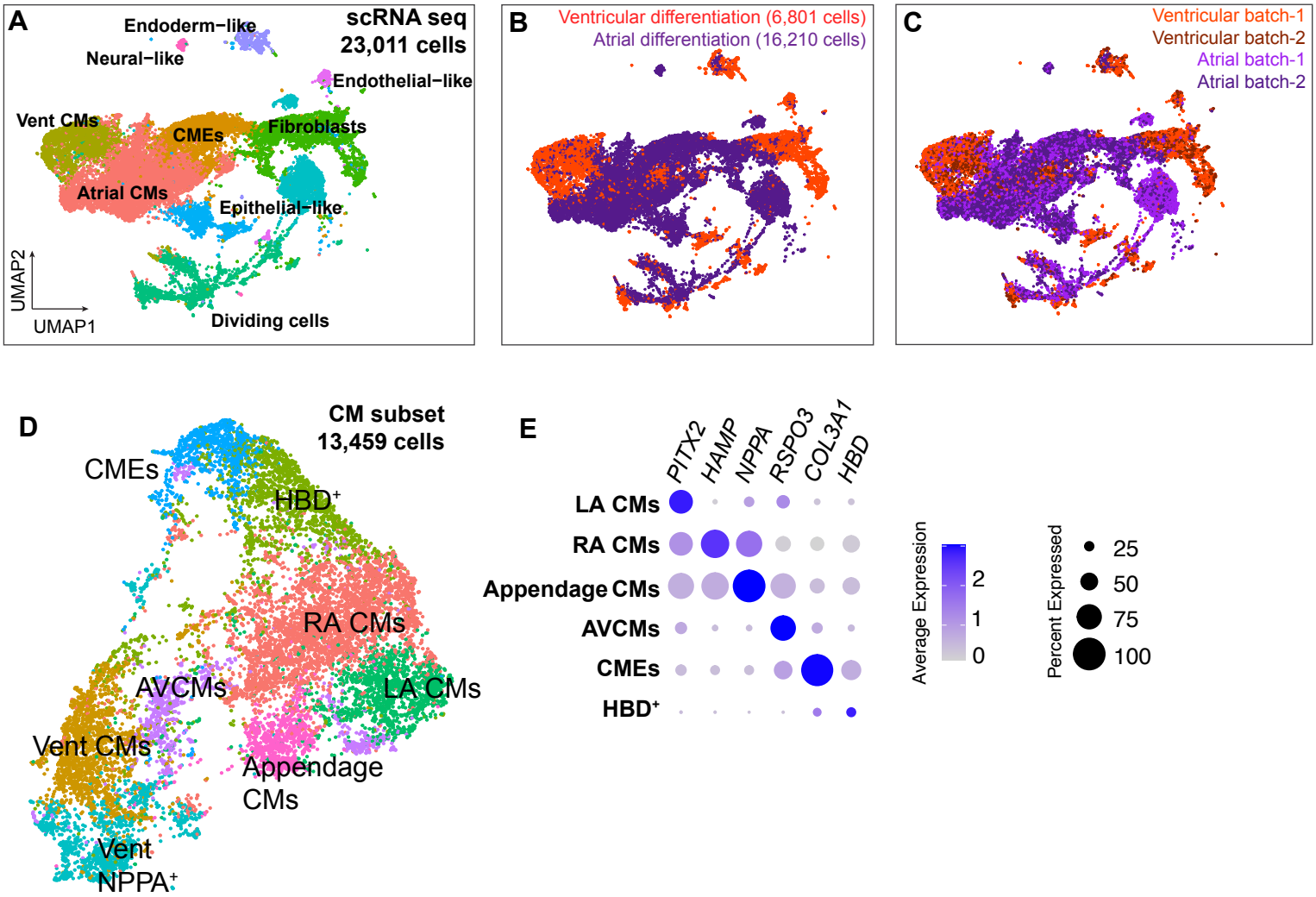
A
scRNA seq
23,011 cells
Endoderm−like
Neural−like
Endothelial−like
Vent CMs
CMEs
Fibroblasts
Atrial CMs
Epithelial−like
Dividing cells
UMAP2
UMAP1
B
Ventricular differentiation (6,801 cells)
Atrial differentiation (16,210 cells)
C
Ventricular batch-1
Ventricular batch-2
Atrial batch-1
Atrial batch-2
D
CM subset
13,459 cells
CMEs
HBD+
RA CMs
AVCMs
LA CMs
Vent CMs
Appendage CMs
Vent NPPA+
E
PITX2
HAMP
NPPA
RSPO3
COL3A1
HBD
LA CMs
RA CMs
Appendage CMs
AVCMs
CMEs
HBD+
Average Expression
2
1
0
Percent Expressed
25
50
75
100

Fig. S2

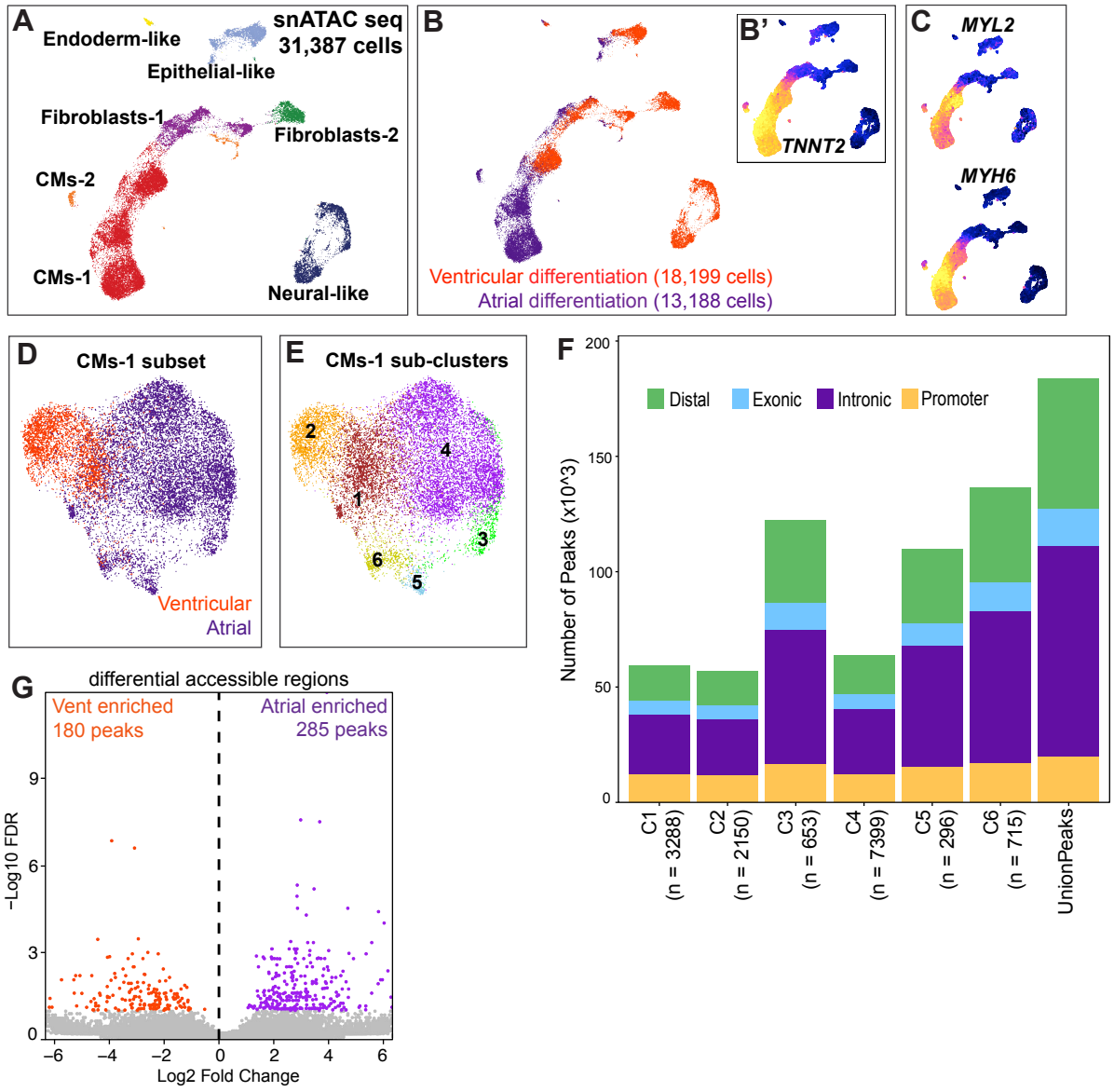
A
snATAC seq
31,387 cells
Endoderm-like
Epithelial-like
Fibroblasts-1
Fibroblasts-2
CMs-2
CMs-1
Neural-like
B
B'
TNNT2
Ventricular differentiation (18,199 cells)
Atrial differentiation (13,188 cells)
C
MYL2
MYH6
D
CMs-1 subset
Ventricular
Atrial
E
CMs-1 sub-clusters
1
2
3
4
5
6
F
Distal
Exonic
Intronic
Promoter
Number of Peaks (x10^3)
C1 (n = 3288)
C2 (n = 2150)
C3 (n = 653)
C4 (n = 7399)
C5 (n = 296)
C6 (n = 715)
UnionPeaks
G
differential accessible regions
Vent enriched
180 peaks
Atrial enriched
285 peaks
−Log10 FDR
Log2 Fold Change

Fig. S3

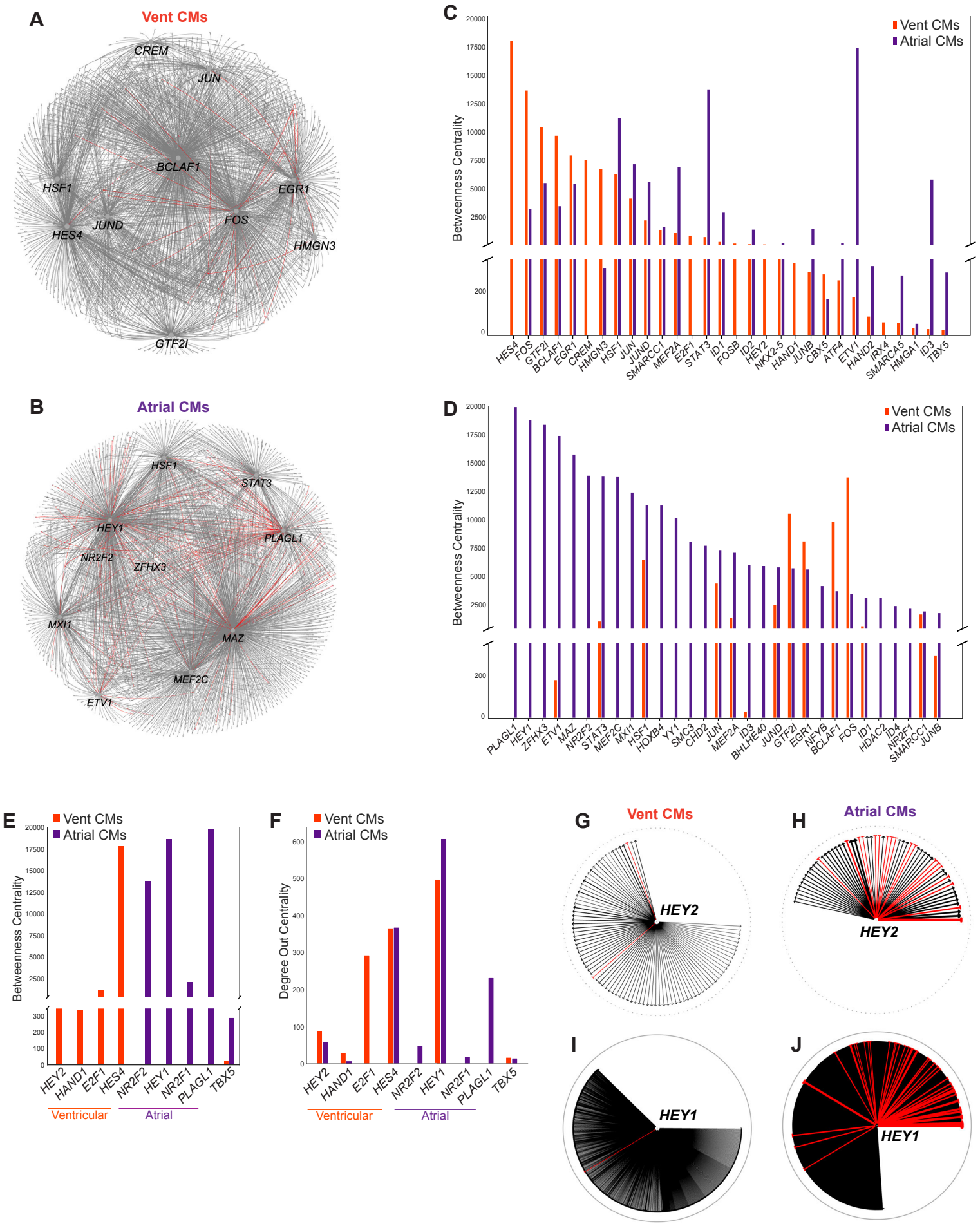
A
Vent CMs
CREM
JUN
BCLAF1
HSF1
EGR1
JUND
FOS
HES4
HMGN3
GTF2I
B
Atrial CMs
HSF1
STAT3
HEY1
PLAGL1
NR2F2
ZFHX3
MXI1
MAZ
MEF2C
ETV1
C
Vent CMs
Atrial CMs
Betweenness Centrality
HES4 FOS GTF2I BCLAF1 EGR1 CREM HMGN3 HSF1 JUN JUND SMARCC1 MEF2A E2F1 STAT3 ID1 FOSB ID2 HEY2 NKX2-5 HAND1 JUNB CBX5 ATF4 ETV1 HAND2 IRX4 SMARCA5 HMGA1 ID3 TBX5
D
Vent CMs
Atrial CMs
Betweenness Centrality
PLAGL1 HEY1 ZFHX3 ETV1 MAZ NR2F2 STAT3 MEF2C MXI1 HSF1 HOXB4 YY1 SMC3 CHD2 JUN MEF2A ID3 BHLHE40 JUND GTF2I EGR1 NFYB BCLAF1 FOS ID1 HDAC2 ID4 NR2F1 SMARCC1 JUNB
E
Vent CMs
Atrial CMs
Betweenness Centrality
HEY2 HAND1 E2F1 HES4 NR2F2 HEY1 NR2F1 PLAGL1 TBX5
Ventricular
Atrial
F
Vent CMs
Atrial CMs
Degree Out Centrality
HEY2 HAND1 E2F1 HES4 NR2F2 HEY1 NR2F1 PLAGL1 TBX5
Ventricular
Atrial
G
Vent CMs
HEY2
H
Atrial CMs
HEY2
I
HEY1
J
HEY1

Fig S4

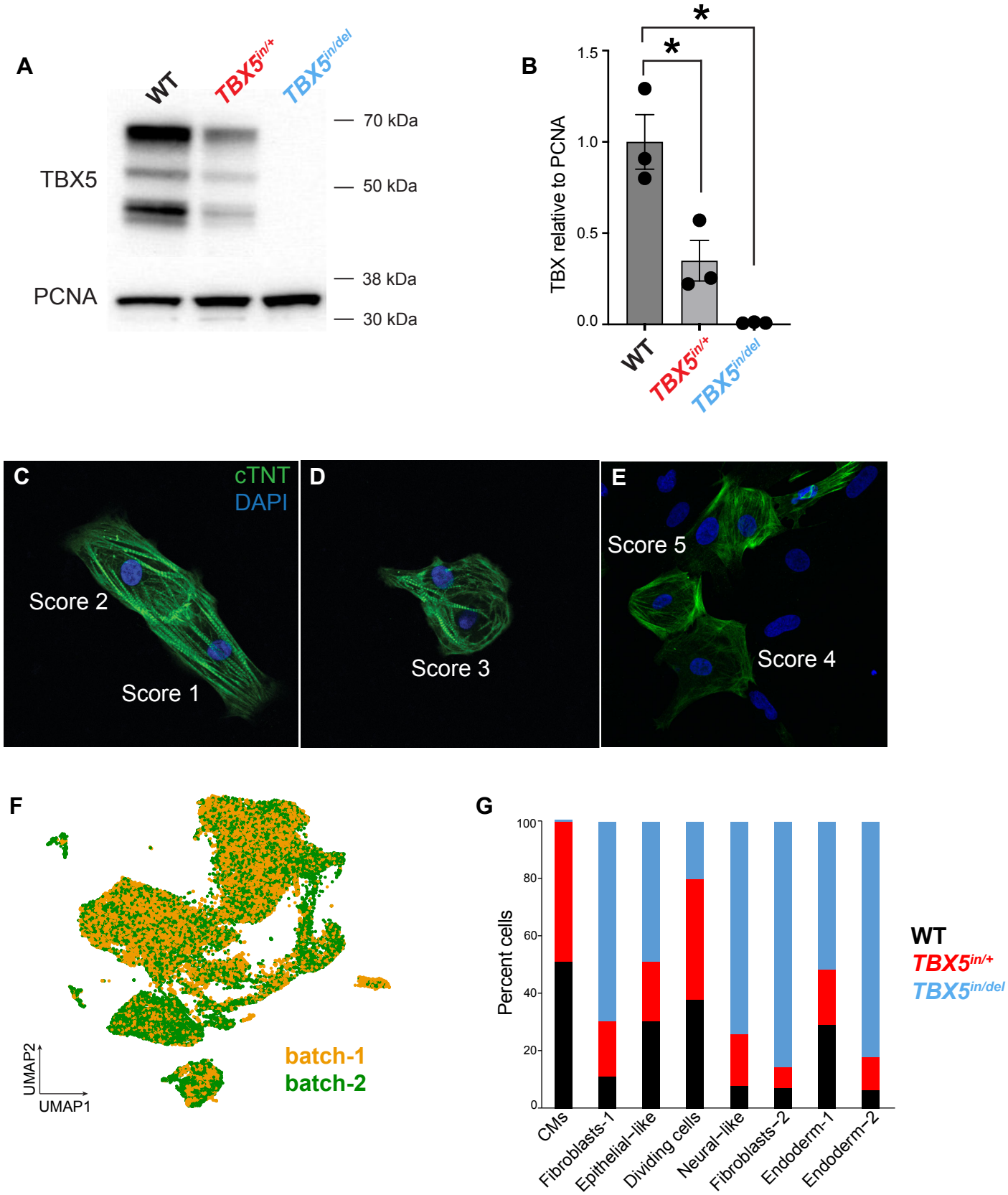
A
WT
TBX5in/+
TBX5in/del
TBX5
PCNA
70 kDa
50 kDa
38 kDa
30 kDa
B
TBX relative to PCNA
1.5
1.0
0.5
0.0
*
*
WT
TBX5in/+
TBX5in/del
C
cTNT
DAPI
Score 2
Score 1
D
Score 3
E
Score 5
Score 4
F
UMAP2
UMAP1
batch-1
batch-2
G
Percent cells
100
80
60
40
20
0
CMs
Fibroblasts-1
Epithelial-like
Dividing cells
Neural-like
Fibroblasts-2
Endoderm-1
Endoderm-2
WT
TBX5in/+
TBX5in/del

Figure 2

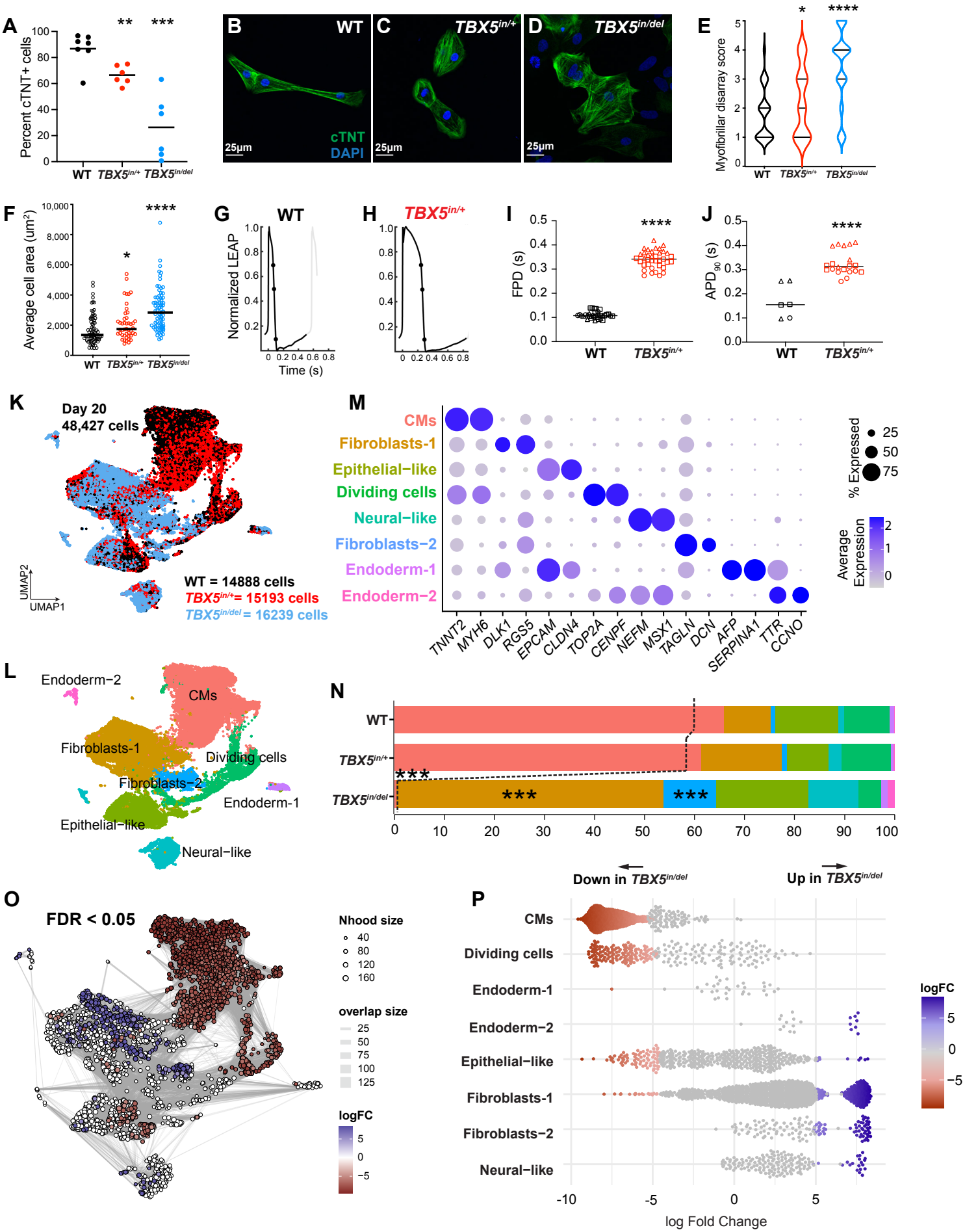
A
Percent cTNT+ cells
WT
TBX5in/+
TBX5in/del
B
WT
C
TBX5in/+
D
TBX5in/del
cTNT
DAPI
25µm
E
Myofibrillar disarray score
F
Average cell area (um²)
G
WT
Normalized LEAP
Time (s)
H
TBX5in/+
I
FPD (s)
J
APD90 (s)
K
Day 20
48,427 cells
UMAP2
UMAP1
WT = 14888 cells
TBX5in/+= 15193 cells
TBX5in/del = 16239 cells
M
CMs
Fibroblasts-1
Epithelial−like
Dividing cells
Neural−like
Fibroblasts−2
Endoderm-1
Endoderm−2
TNNT2
MYH6
DLK1
RGS5
EPCAM
CLDN4
TOP2A
CENPF
NEFM
MSX1
TAGLN
DCN
AFP
SERPINA1
TTR
CCNO
% Expressed
Average Expression
L
Endoderm−2
CMs
Fibroblasts-1
Dividing cells
Fibroblasts−2
Endoderm-1
Epithelial−like
Neural−like
N
WT
TBX5in/+
TBX5in/del
Down in TBX5in/del
Up in TBX5in/del
O
FDR < 0.05
Nhood size
overlap size
logFC
P
CMs
Dividing cells
Endoderm-1
Endoderm−2
Epithelial−like
Fibroblasts-1
Fibroblasts−2
Neural−like
log Fold Change
logFC

Figure 3

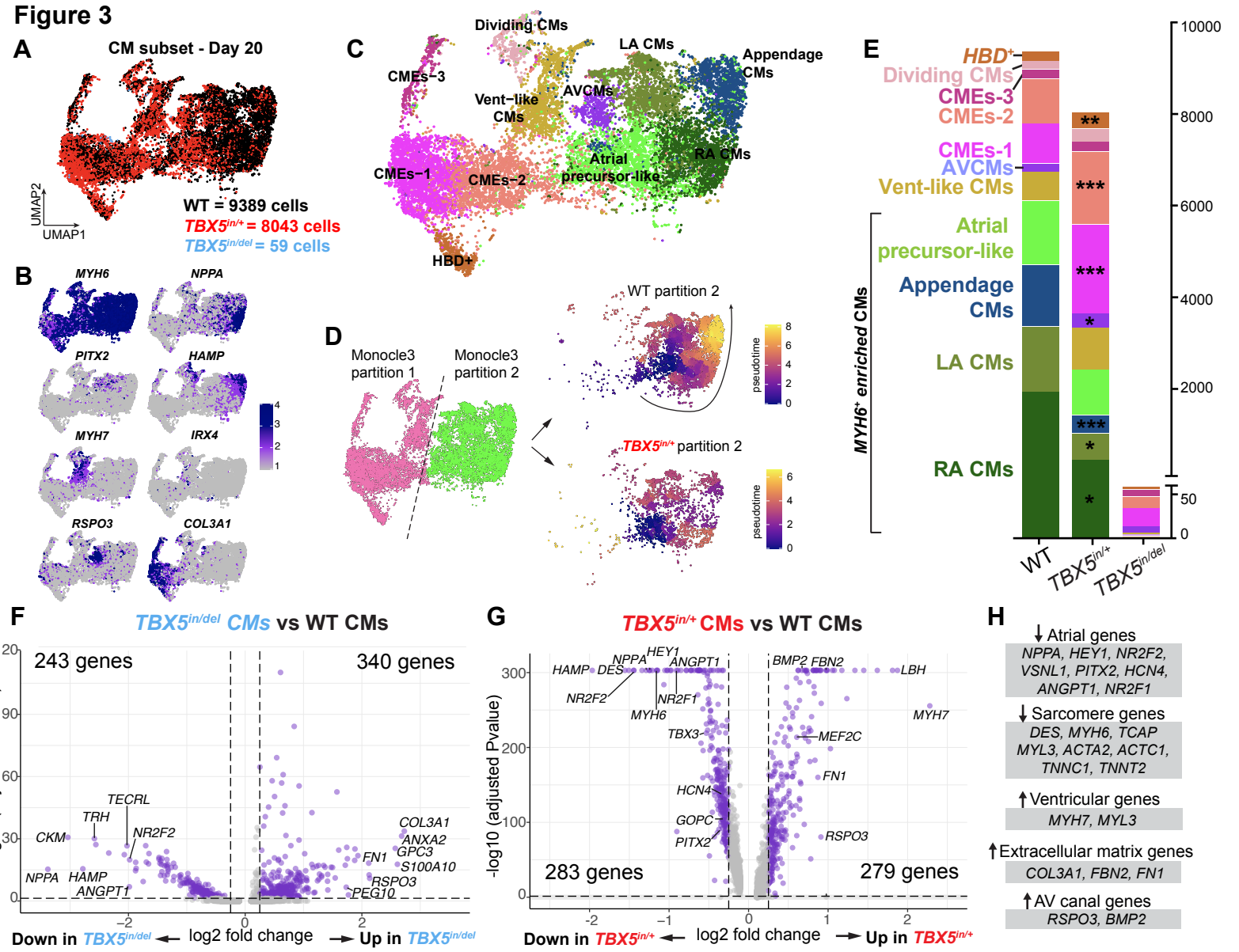
A
CM subset - Day 20
UMAP2
UMAP1
WT = 9389 cells
TBX5in/+ = 8043 cells
TBX5in/del = 59 cells
B
MYH6
NPPA
PITX2
HAMP
MYH7
IRX4
RSPO3
COL3A1
C
Dividing CMs
LA CMs
Appendage CMs
CMEs−3
Vent−like CMs
AVCMs
Atrial precursor-like
RA CMs
CMEs−1
CMEs−2
HBD+
D
Monocle3 partition 1
Monocle3 partition 2
WT partition 2
TBX5in/+ partition 2
pseudotime
E
HBD+
Dividing CMs
CMEs-3
CMEs-2
CMEs-1
AVCMs
Vent-like CMs
Atrial precursor-like
Appendage CMs
LA CMs
RA CMs
MYH6+ enriched CMs
WT
TBX5in/+
TBX5in/del
F
TBX5in/del CMs vs WT CMs
243 genes
340 genes
-log10 (adjusted Pvalue)
TECRL
TRH
CKM
NR2F2
NPPA
HAMP
ANGPT1
COL3A1
ANXA2
GPC3
S100A10
FN1
RSPO3
PEG10
Down in TBX5in/del
log2 fold change
Up in TBX5in/del
G
TBX5in/+ CMs vs WT CMs
HAMP
DES
NPPA
HEY1
ANGPT1
NR2F2
NR2F1
MYH6
TBX3
HCN4
GOPC
PITX2
BMP2
FBN2
LBH
MYH7
MEF2C
FN1
RSPO3
283 genes
279 genes
Down in TBX5in/+
log2 fold change
Up in TBX5in/+
H
Atrial genes
NPPA, HEY1, NR2F2, VSNL1, PITX2, HCN4, ANGPT1, NR2F1
Sarcomere genes
DES, MYH6, TCAP MYL3, ACTA2, ACTC1, TNNC1, TNNT2
Ventricular genes
MYH7, MYL3
Extracellular matrix genes
COL3A1, FBN2, FN1
AV canal genes
RSPO3, BMP2
I
AF-risk genes
1482
44
240
50
228
33
272
Genes altered in TBX5in/+
3.8-fold enrichment
p < 3.030e-29
Genes altered in TBX5in/del
3.2-fold enrichment
p < 2.730e-21
J
ASD-risk genes
108
8
276
4
274
2
303
Genes altered in TBX5in/+
6.4-fold enrichment
p < 4.290e-07
Genes altered in TBX5in/del
3.1-fold enrichment
p < 0.014
K
CHD-risk genes
407
19
256
21
257
3
302
Genes altered in TBX5in/+
5.8-fold enrichment
p < 5.967e-19
Genes altered in TBX5in/del
3.3-fold enrichment
p < 3.367e-07
L
WT
TBX5in/+
CHD genes
NR2F2
CFC1
RABGAP1L
COL2A1
RPS24
SMAD6
RPL5
JAG1
TBX20
FGFR2
GPC6
GLI3
FGFR1
KAT6B
ANKRD1
COL5A2
VCAN
AHNAK
WLS
HAND1
MEIS2
COL5A1
PBX1
ACTB
CDKN1C
GPC3
PITX2
CHD & AF genes
ACTC1
MYH6
MYH7
ACTA2
PDGFRA
PRKAG2
TBX3
MYOCD
BMP2
IGFBP7
COL1A1
FBN2
COL3A1
AF genes
DES
CKM
ANGPT1
ATP2A2
ATP1A2
CTSL
CSRP3
GYPC
CMYA5
GPX3
ADM
FBXO32
FRMD4B
GAS5
ARHGAP26
CAMK2D
GOPC
CPNE5
ERBB4
ERBB2
CCND1
HAND2-AS1
CUL4A
CACNA1D
ACTN2
CPM
EZR
CRYAB
ATP6AP2
FKBP1B
ATP1A1
GSTP1
CST3
EIF4EBP1
BSCL2
APOE
BTG3
ACTG1
CNTN5
FN1
NPPA
MYL3
TRIM55
LGALS3
TNNT2
SLC8A1
NEXN
PANCR
TNNI3
TPM1
MLLT3
SERPINI1
PLXNA4
HSPB2
LRRC10
SPEG
MYO18B
MYL4
PPP2R2B
HCN4
SLC25A4
SSPN
SYNE2
VIM
VKORC1
PPM1K
HLA-C
ZNF385D
SLC2A1
PKP2
KCNQ1OT1
TGFB2
NRP1
TIMP1
ID1
VCAM1
IGFBP2
SNCA
TAGLN
PLAT
% Expressed
25
50
75
100
Average Expression
0.4
0.0
−0.4
M
WT
TBX5in/+
TBX5in/del
CHD genes
NR2F2
CFC1
RABGAP1L
COL2A1
RPS24
SMAD6
JAG1
VCAN
HAND1
MEIS2
ACTB
CDKN1C
GPC3
CHD & AF genes
MYH6
MYOCD
PDGFRA
PRKAG2
TBX3
COL1A1
COL3A1
AF genes
FBXO32
GAS5
PLXNA4
HSPB2
LRRC10
SPEG
MYO18B
HCN4
CPNE5
SLC25A4
ERBB4
HAND2-AS1
CACNA1D
ACTN2
ATP1A1
CKM
NPPA
ANGPT1
TRIM55
LGALS3
ATP2A2
TNNT2
ATP1A2
CTSL
CSRP3
SLC8A1
CMYA5
GPX3
ADM
TNNI3
TPM1
MLLT3
VIM
GSTP1
CST3
EIF4EBP1
TIMP1
ACTG1
CNTN5
TAGLN
FN1
PLAT
% Expressed
25
50
75
100
Average Expression
1.0
0.0
−1.0

Fig S5

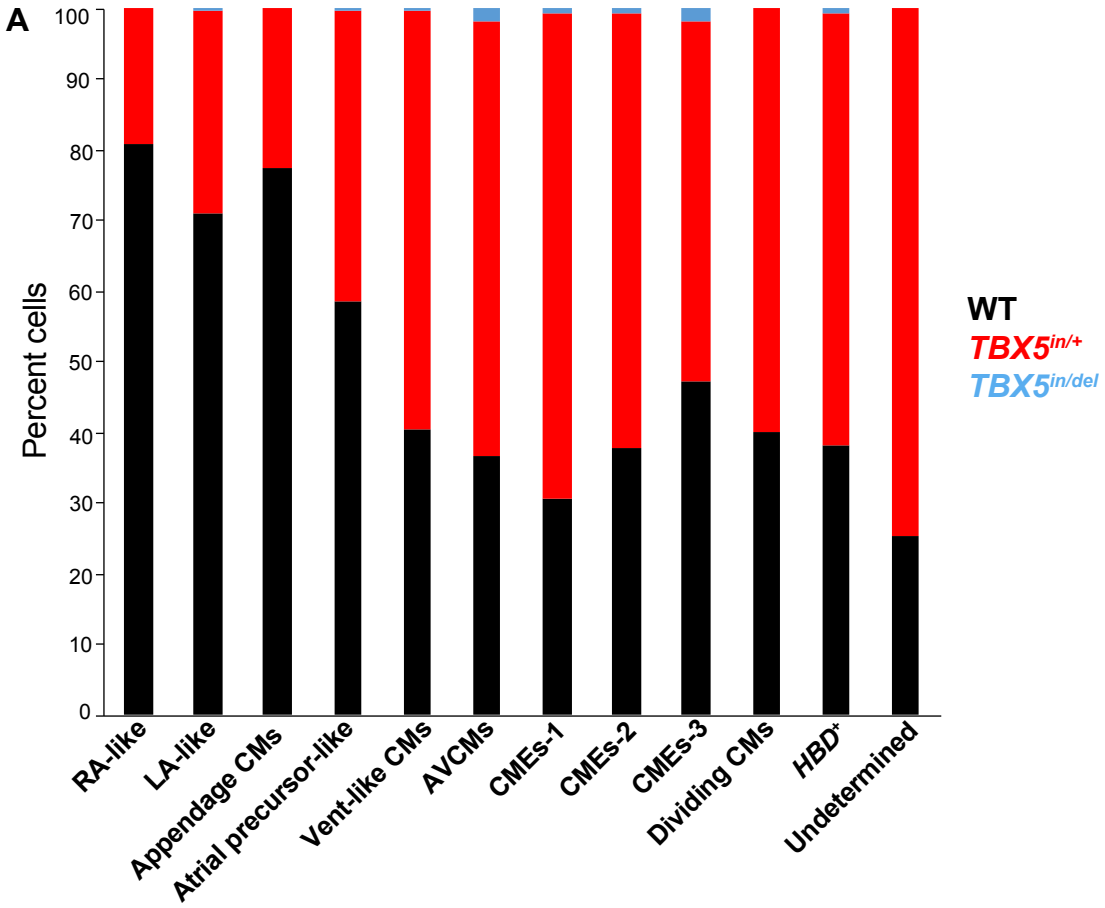
A
Percent cells
100
90
80
70
60
50
40
30
20
10
0
RA-like
LA-like
Appendage CMs
Atrial precursor-like
Vent-like CMs
AVCMs
CMEs-1
CMEs-2
CMEs-3
Dividing CMs
HBD+
Undetermined
WT
TBX5in/+
TBX5in/del

Figure 4

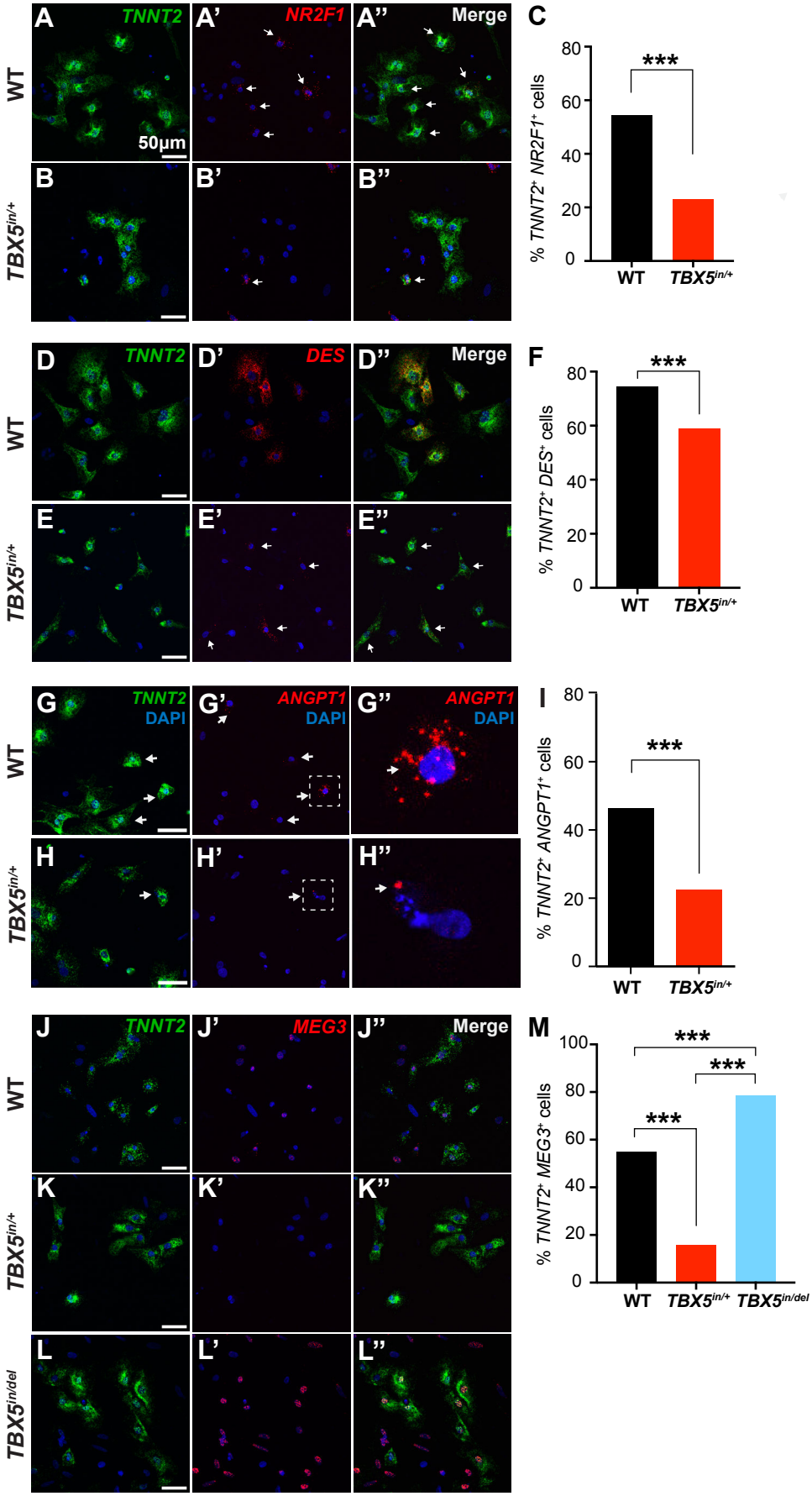
A
TNNT2
A'
NR2F1
A''
Merge
WT
50µm
B
B'
B''
TBX5in/+
C
% TNNT2+ NR2F1+ cells
***
WT
TBX5in/+
D
TNNT2
D'
DES
D''
Merge
E
E'
E''
F
% TNNT2+ DES+ cells
G
TNNT2
DAPI
G'
ANGPT1
DAPI
G''
ANGPT1
DAPI
H
H'
H''
I
% TNNT2+ ANGPT1+ cells
J
TNNT2
J'
MEG3
J''
Merge
K
K'
K''
L
L'
L''
TBX5in/del
M
% TNNT2+ MEG3+ cells
WT
TBX5in/+
TBX5in/del

Fig. S6

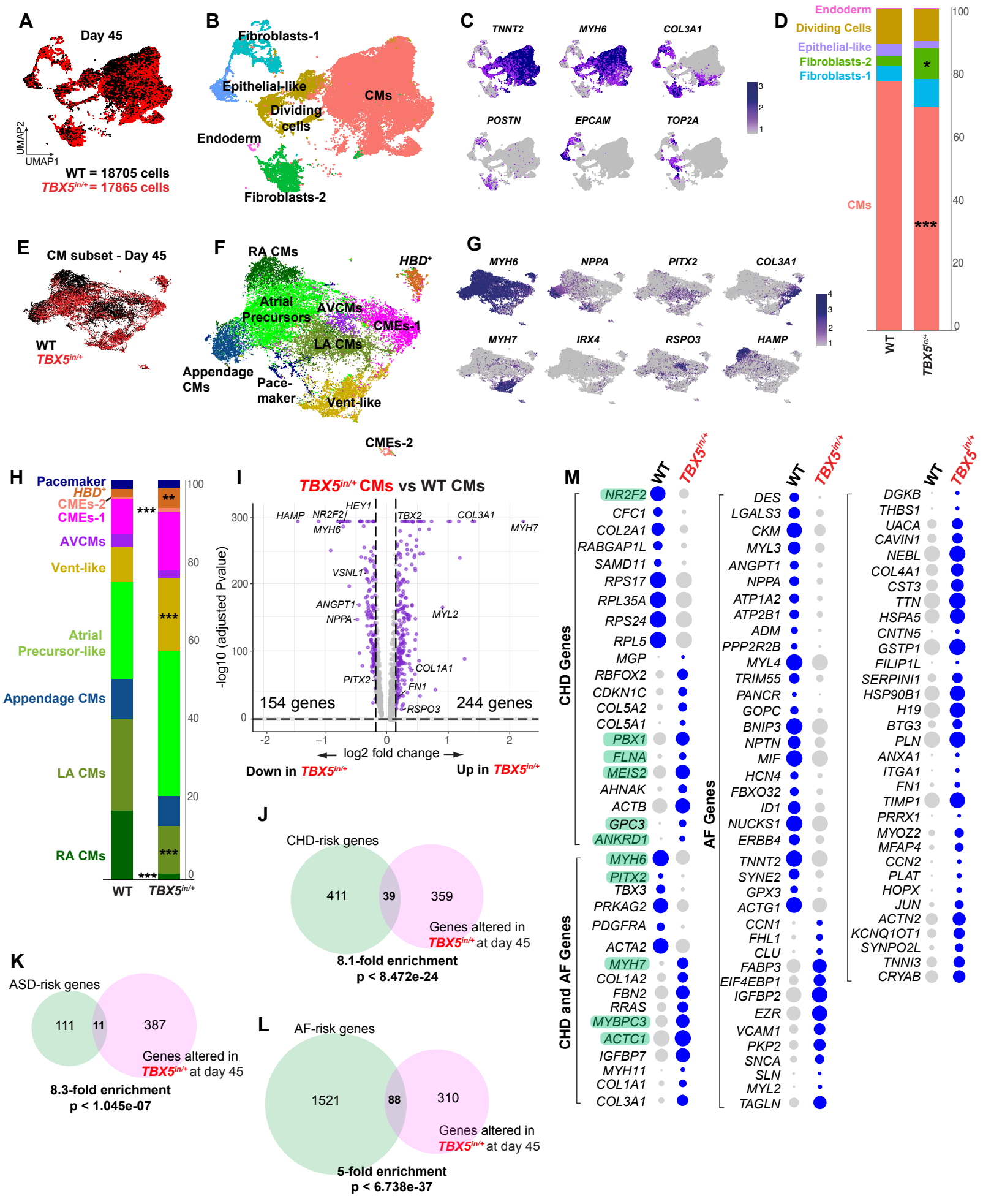
A
Day 45
UMAP2
UMAP1
WT = 18705 cells
TBX5in/+ = 17865 cells
B
Fibroblasts-1
Epithelial-like
Dividing cells
CMs
Endoderm
Fibroblasts-2
C
TNNT2
MYH6
COL3A1
POSTN
EPCAM
TOP2A
D
Endoderm
Dividing Cells
Epithelial-like
Fibroblasts-2
Fibroblasts-1
CMs
WT
TBX5in/+
E
CM subset - Day 45
WT
TBX5in/+
F
RA CMs
HBD+
Atrial Precursors
AVCMs
CMEs-1
LA CMs
Appendage CMs
Pace-maker
Vent-like
CMEs-2
G
MYH6
NPPA
PITX2
COL3A1
MYH7
IRX4
RSPO3
HAMP
H
Pacemaker
HBD+
CMEs-2
CMEs-1
AVCMs
Vent-like
Atrial Precursor-like
Appendage CMs
LA CMs
RA CMs
WT
TBX5in/+
I
TBX5in/+ CMs vs WT CMs
-log10 (adjusted Pvalue)
HAMP
NR2F2
HEY1
MYH6
TBX2
COL3A1
MYH7
VSNL1
ANGPT1
NPPA
MYL2
COL1A1
PITX2
FN1
RSPO3
154 genes
244 genes
log2 fold change
Down in TBX5in/+
Up in TBX5in/+
J
CHD-risk genes
411
39
359
Genes altered in TBX5in/+ at day 45
8.1-fold enrichment
p < 8.472e-24
K
ASD-risk genes
111
11
387
Genes altered in TBX5in/+ at day 45
8.3-fold enrichment
p < 1.045e-07
L
AF-risk genes
1521
88
310
Genes altered in TBX5in/+ at day 45
5-fold enrichment
p < 6.738e-37
M
WT
TBX5in/+
CHD Genes
NR2F2
CFC1
COL2A1
RABGAP1L
SAMD11
RPS17
RPL35A
RPS24
RPL5
MGP
RBFOX2
CDKN1C
COL5A2
COL5A1
PBX1
FLNA
MEIS2
AHNAK
ACTB
GPC3
ANKRD1
CHD and AF Genes
MYH6
PITX2
TBX3
PRKAG2
PDGFRA
ACTA2
MYH7
COL1A2
FBN2
RRAS
MYBPC3
ACTC1
IGFBP7
MYH11
COL1A1
COL3A1
AF Genes
DES
LGALS3
CKM
MYL3
ANGPT1
NPPA
ATP1A2
ATP2B1
ADM
PPP2R2B
MYL4
TRIM55
PANCR
GOPC
BNIP3
NPTN
MIF
HCN4
FBXO32
ID1
NUCKS1
ERBB4
TNNT2
SYNE2
GPX3
ACTG1
CCN1
FHL1
CLU
FABP3
EIF4EBP1
IGFBP2
EZR
VCAM1
PKP2
SNCA
SLN
MYL2
TAGLN
DGKB
THBS1
UACA
CAVIN1
NEBL
COL4A1
CST3
TTN
HSPA5
CNTN5
GSTP1
FILIP1L
SERPINI1
HSP90B1
H19
BTG3
PLN
ANXA1
ITGA1
FN1
TIMP1
PRRX1
MYOZ2
MFAP4
CCN2
PLAT
HOPX
JUN
ACTN2
KCNQ1OT1
SYNPO2L
TNNI3
CRYAB

Fig. S7

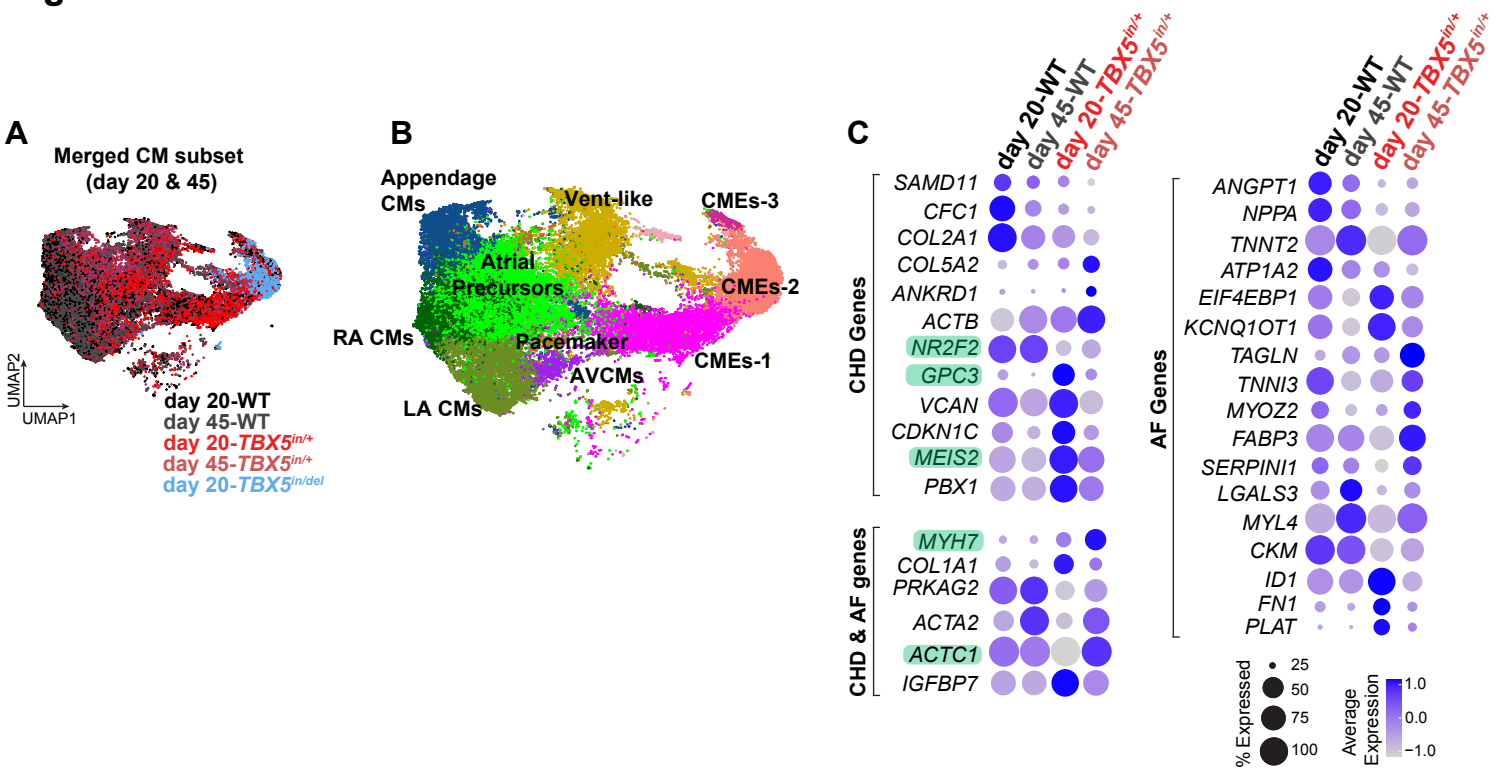
A
Merged CM subset
(day 20 & 45)
UMAP2
UMAP1
day 20-WT
day 45-WT
day 20-TBX5in/+
day 45-TBX5in/+
day 20-TBX5in/del
B
Appendage CMs
Vent-like
CMEs-3
Atrial Precursors
CMEs-2
RA CMs
Pacemaker
CMEs-1
AVCMs
LA CMs
C
day 20-WT
day 45-WT
day 20-TBX5in/+
day 45-TBX5in/+
CHD Genes
SAMD11
CFC1
COL2A1
COL5A2
ANKRD1
ACTB
NR2F2
GPC3
VCAN
CDKN1C
MEIS2
PBX1
CHD & AF genes
MYH7
COL1A1
PRKAG2
ACTA2
ACTC1
IGFBP7
AF Genes
ANGPT1
NPPA
TNNT2
ATP1A2
EIF4EBP1
KCNQ1OT1
TAGLN
TNNI3
MYOZ2
FABP3
SERPINI1
LGALS3
MYL4
CKM
ID1
FN1
PLAT
% Expressed
25
50
75
100
Average Expression
1.0
0.0
−1.0

Figure 5

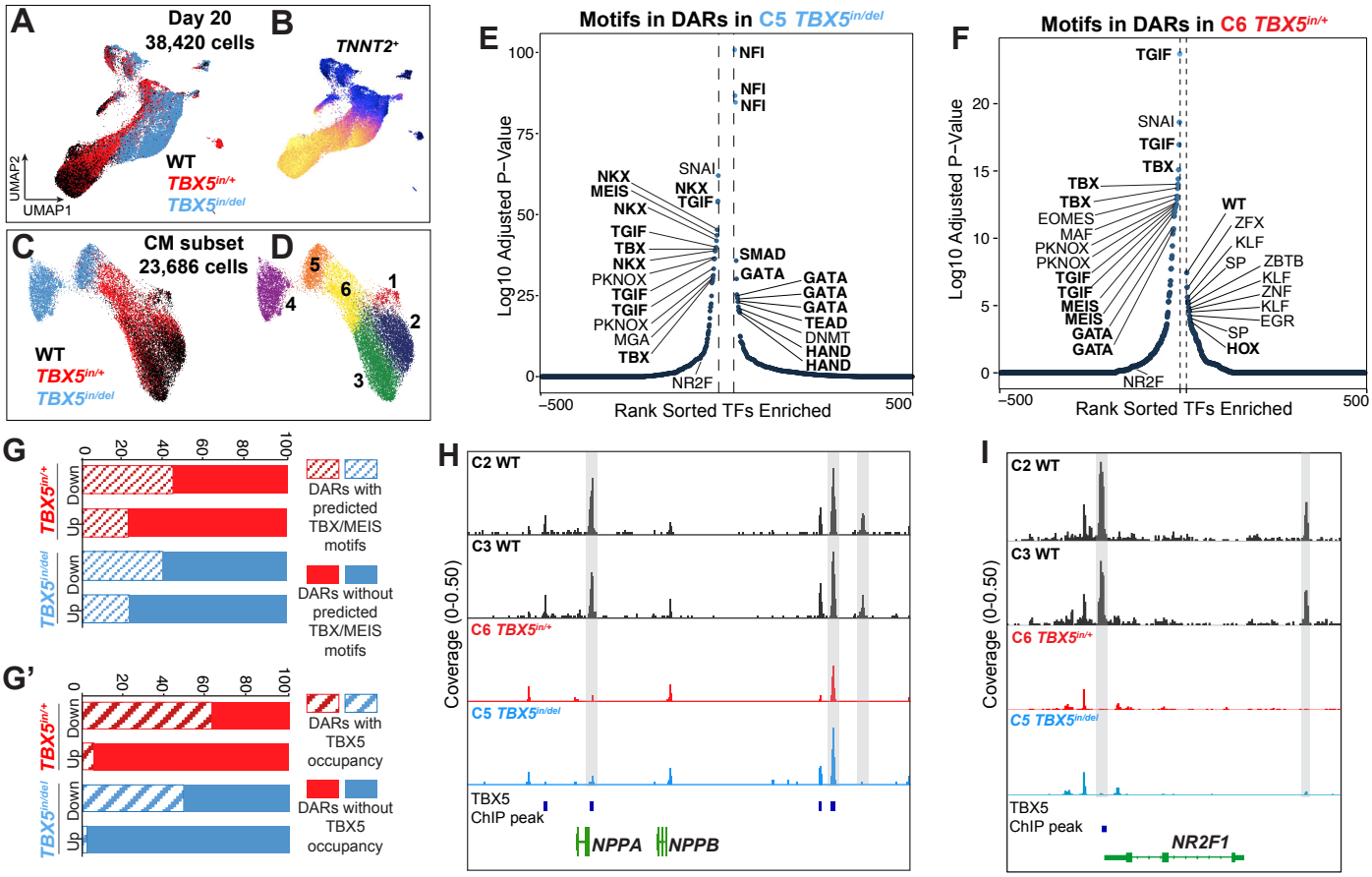
A
Day 20
38,420 cells
WT
TBX5in/+
TBX5in/del
UMAP2
UMAP1
B
TNNT2+
C
CM subset
23,686 cells
WT
TBX5in/+
TBX5in/del
D
1
2
3
4
5
6
E
Motifs in DARs in C5 TBX5in/del
Log10 Adjusted P−Value
Rank Sorted TFs Enriched
NFI
NFI
NFI
SNAI
NKX
MEIS
NKX
TGIF
NKX
TGIF
TBX
NKX
PKNOX
TGIF
TGIF
PKNOX
MGA
TBX
NR2F
SMAD
GATA
GATA
GATA
GATA
GATA
TEAD
DNMT
HAND
HAND
F
Motifs in DARs in C6 TBX5in/+
Log10 Adjusted P−Value
Rank Sorted TFs Enriched
TGIF
SNAI
TGIF
TBX
TBX
TBX
EOMES
MAF
PKNOX
PKNOX
TGIF
TGIF
MEIS
MEIS
GATA
GATA
NR2F
WT
ZFX
KLF
SP
ZBTB
KLF
ZNF
KLF
EGR
SP
HOX
G
TBX5in/+
TBX5in/del
Down
Up
DARs with predicted TBX/MEIS motifs
DARs without predicted TBX/MEIS motifs
G'
DARs with TBX5 occupancy
DARs without TBX5 occupancy
H
C2 WT
C3 WT
C6 TBX5in/+
C5 TBX5in/del
Coverage (0-0.50)
TBX5 ChIP peak
NPPA
NPPB
I
C2 WT
C3 WT
C6 TBX5in/+
C5 TBX5in/del
Coverage (0-0.50)
TBX5 ChIP peak
NR2F1

Fig. S8

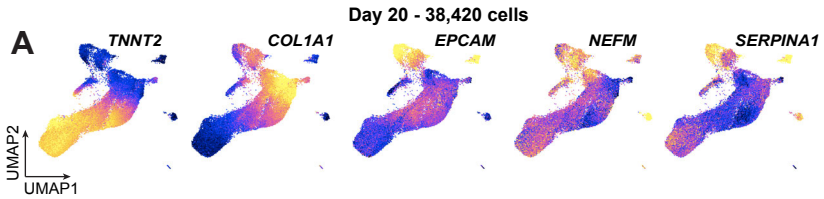
A
Day 20 - 38,420 cells
TNNT2
COL1A1
EPCAM
NEFM
SERPINA1
UMAP2
UMAP1

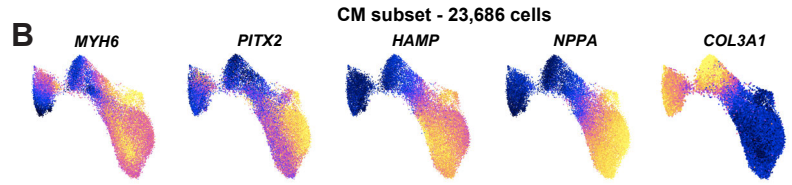
B
CM subset - 23,686 cells
MYH6
PITX2
HAMP
NPPA
COL3A1

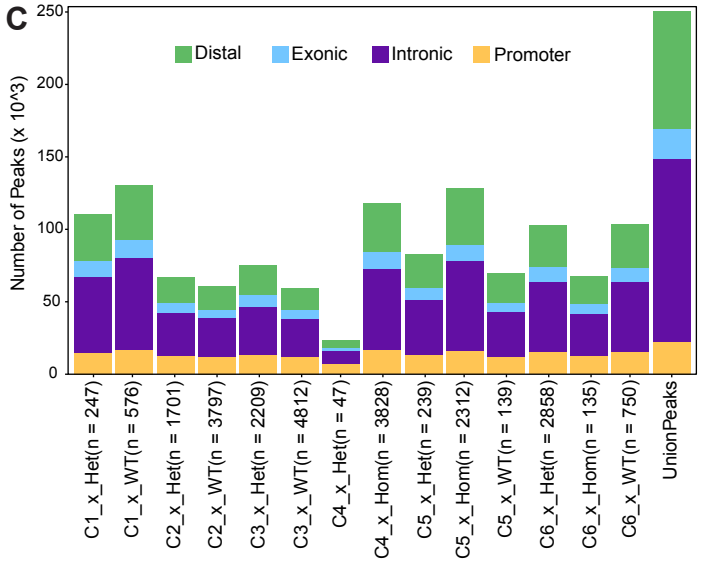
C
Distal
Exonic
Intronic
Promoter
Number of Peaks (x 10^3)
0
50
100
150
200
250
C1_x_Het(n = 247)
C1_x_WT(n = 576)
C2_x_Het(n = 1701)
C2_x_WT(n = 3797)
C3_x_Het(n = 2209)
C3_x_WT(n = 4812)
C4_x_Het(n = 47)
C4_x_Hom(n = 3828)
C5_x_Het(n = 239)
C5_x_Hom(n = 2312)
C5_x_WT(n = 139)
C6_x_Het(n = 2858)
C6_x_Hom(n = 135)
C6_x_WT(n = 750)
UnionPeaks

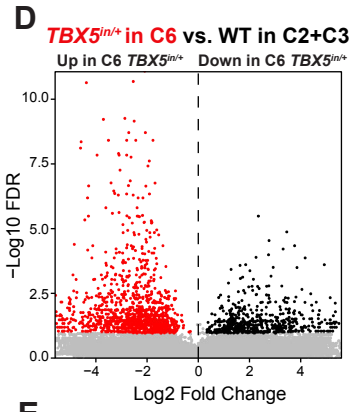
D
TBX5in/+ in C6 vs. WT in C2+C3
Up in C6 TBX5in/+
Down in C6 TBX5in/+
−Log10 FDR
Log2 Fold Change

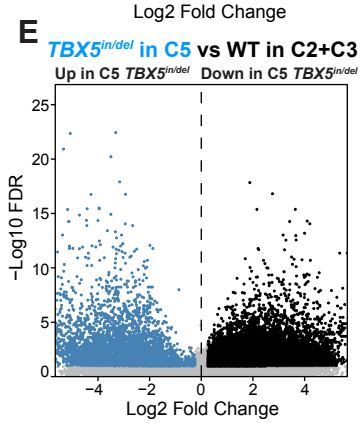
E
TBX5in/del in C5 vs WT in C2+C3
Up in C5 TBX5in/del
Down in C5 TBX5in/del
−Log10 FDR
Log2 Fold Change

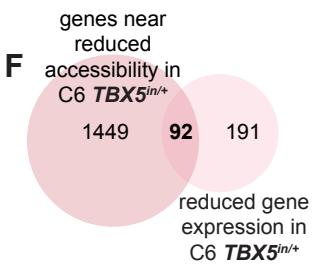
F
genes near reduced accessibility in C6 TBX5in/+
1449
92
191
reduced gene expression in C6 TBX5in/+

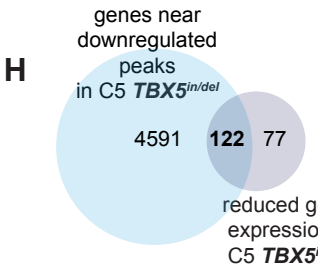
H
genes near downregulated peaks in C5 TBX5in/del
4591
122
77
reduced gene expression in C5 TBX5in/del

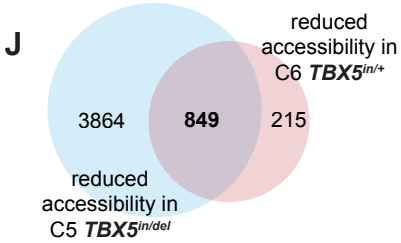
J
reduced accessibility in C6 TBX5in/+
3864
849
215
reduced accessibility in C5 TBX5in/del

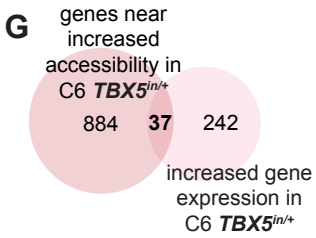
G
genes near increased accessibility in C6 TBX5in/+
884
37
242
increased gene expression in C6 TBX5in/+

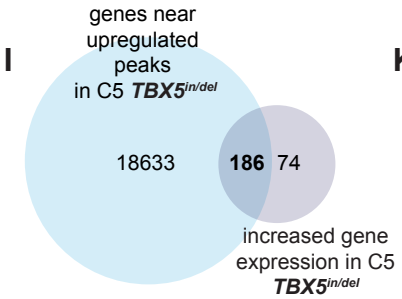
I
genes near upregulated peaks in C5 TBX5in/del
18633
186
74
increased gene expression in C5 TBX5in/del

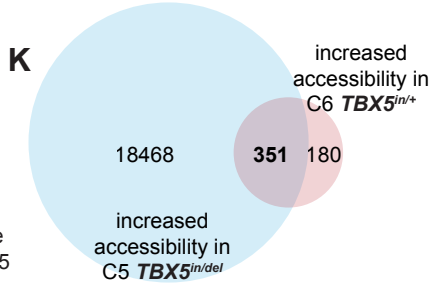
K
increased accessibility in C6 TBX5in/+
18468
351
180
increased accessibility in C5 TBX5in/del

Figure 6

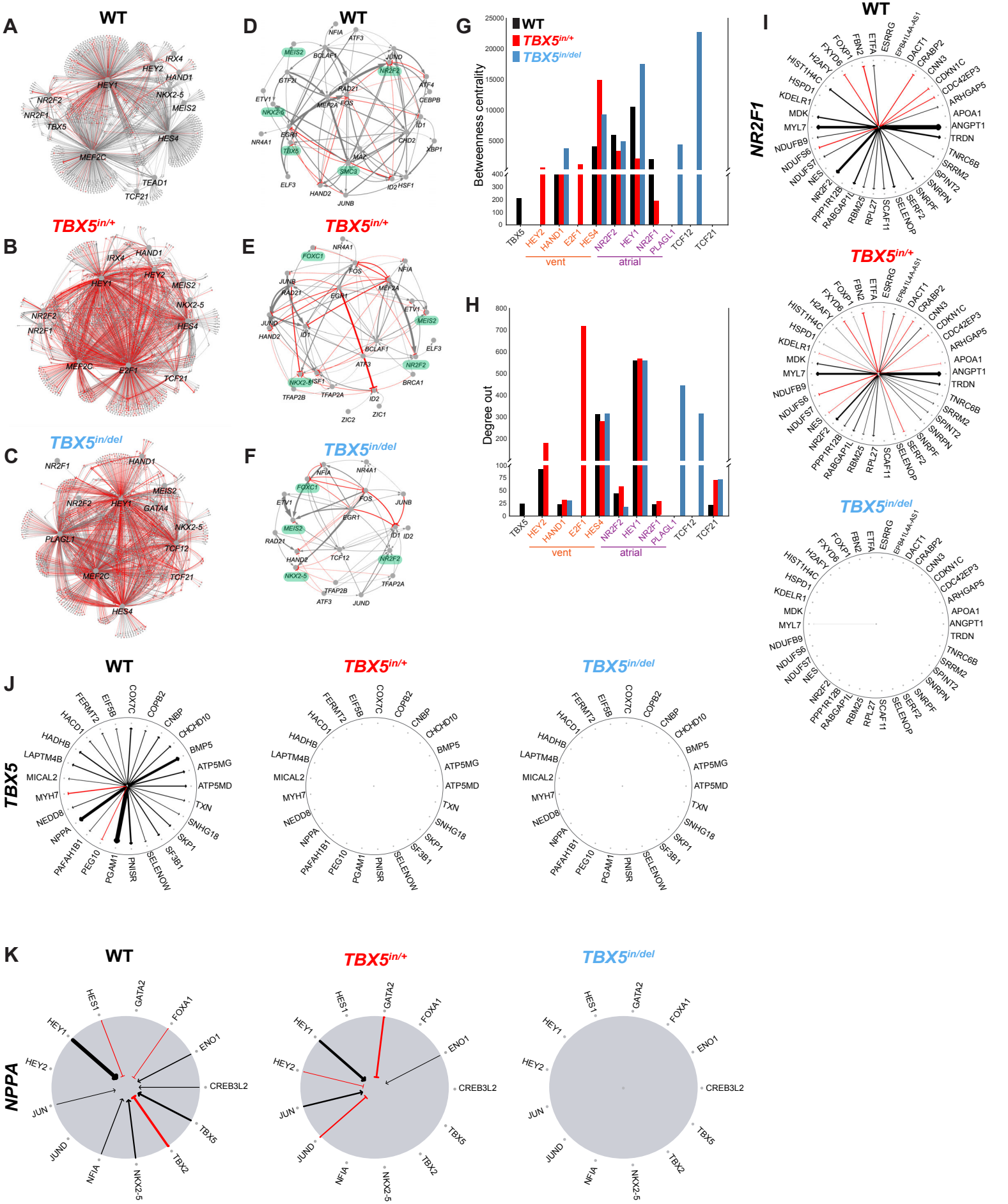
A
WT
IRX4
HEY2
HAND1
HEY1
NKX2-5
NR2F2
MEIS2
NR2F1
TBX5
HES4
MEF2C
TEAD1
TCF21
B
TBX5in/+
IRX4
HAND1
HEY1
HEY2
MEIS2
NKX2-5
NR2F2
HES4
NR2F1
MEF2C
E2F1
TCF21
C
TBX5in/del
NR2F1
HAND1
MEIS2
NR2F2
HEY1
GATA4
NKX2-5
PLAGL1
TCF12
MEF2C
TCF21
HES4
D
WT
NFIA
ATF3
MEIS2
BCLAF1
JUND
NR2F2
GTF2I
RAD21
ATF4
ETV1
MEF2A
FOS
CEBPB
NKX2-5
ID1
NR4A1
EGR1
CHD2
TBX5
XBP1
MAZ
SMC3
ELF3
ID2
HSF1
HAND2
JUNB
E
TBX5in/+
NR4A1
FOXC1
FOS
NFIA
JUNB
MEF2A
RAD21
EGR1
ETV1
JUND
MEIS2
HAND2
ID1
ELF3
BCLAF1
ATF3
NR2F2
NKX2-5
HSF1
BRCA1
TFAP2B
TFAP2A
ID2
ZIC2
ZIC1
F
TBX5in/del
NR4A1
NFIA
FOXC1
FOS
JUNB
ETV1
EGR1
MEIS2
ID1
ID2
RAD21
HAND2
TCF12
NR2F2
NKX2-5
TFAP2B
TFAP2A
ATF3
JUND
G
WT
TBX5in/+
TBX5in/del
Betweenness centrality
25000
20000
15000
10000
5000
400
300
200
100
0
TBX5
HEY2
HAND1
E2F1
HES4
NR2F2
HEY1
NR2F1
PLAGL1
TCF12
TCF21
vent
atrial
H
Degree out
800
700
600
500
400
300
200
100
75
50
25
0
TBX5
HEY2
HAND1
E2F1
HES4
NR2F2
HEY1
NR2F1
PLAGL1
TCF12
TCF21
vent
atrial
I
WT
NR2F1
EPB41L4A-AS1
ESRRG
ETFA
FBN2
FOXP1
FXYD6
H2AFY
HIST1H4C
HSPD1
KDELR1
MDK
MYL7
NDUFB9
NDUFS6
NDUFS7
NES
NR2F2
PPP1R12B
RABGAP1L
RBM25
RPL27
SCAF11
SELENOP
SERF2
SNRPF
SNRPN
SPINT2
SRRM2
TNRC6B
TRDN
ANGPT1
APOA1
ARHGAP5
CDC42EP3
CDKN1C
CNN3
CRABP2
DACT1
TBX5in/+
TBX5in/del
J
WT
TBX5
COXTC
COPB2
CNBP
CHCHD10
BMP5
ATP5MG
ATP5MD
TXN
SNHG18
SKP1
SF3B1
SELENOW
PNISR
PGAM1
PEG10
PAFAH1B1
NPPA
NEDD8
MYH7
MICAL2
LAPTM4B
HADHB
HACD1
FERMT2
EIF5B
TBX5in/+
TBX5in/del
K
WT
NPPA
HES1
GATA2
FOXA1
HEY1
ENO1
HEY2
CREB3L2
JUN
TBX5
JUND
TBX2
NFIA
NKX2-5
TBX5in/+
TBX5in/del

Fig. S9

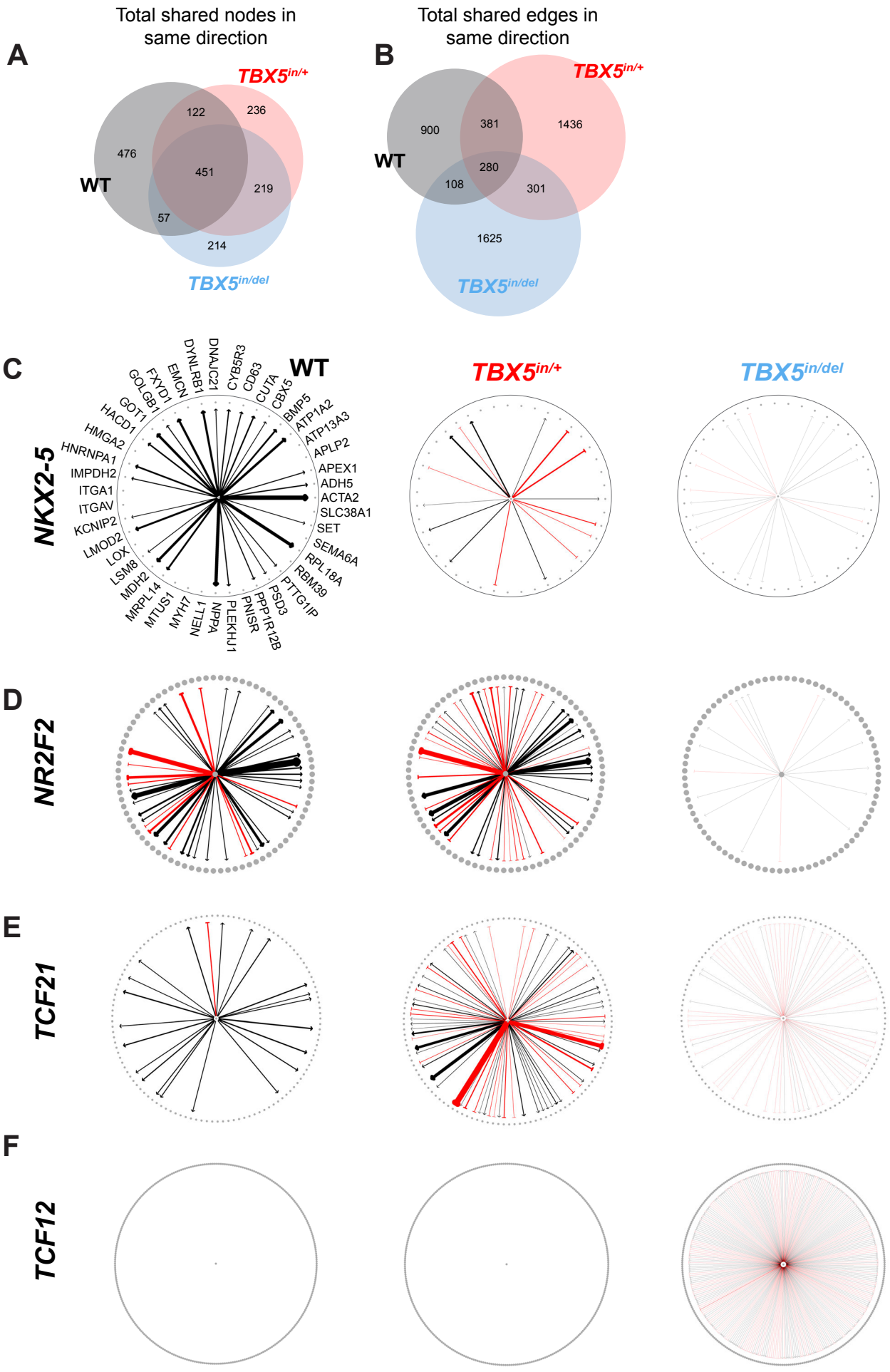
A
Total shared nodes in same direction
TBX5in/+
WT
TBX5in/del
476
122
236
451
219
57
214
B
Total shared edges in same direction
TBX5in/+
WT
TBX5in/del
900
381
1436
280
108
301
1625
C
NKX2-5
WT
TBX5in/+
TBX5in/del
DNAJC21
CYB5R3
CD63
CUTA
CBX5
BMP5
ATP1A2
ATP13A3
APLP2
APEX1
ADH5
ACTA2
SLC38A1
SET
SEMA6A
RPL18A
RBM39
PTTG1IP
PSD3
PPP1R12B
PNISR
PLEKHJ1
NPPA
NELL1
MYH7
MTUS1
MRPL14
MDH2
LSM8
LOX
LMOD2
KCNIP2
ITGAV
ITGA1
IMPDH2
HNRNPA1
HMGA2
HACD1
GOT1
GOLGB1
FXYD1
EMCN
DYNLRB1
D
NR2F2
E
TCF21
F
TCF12

Fig. S10

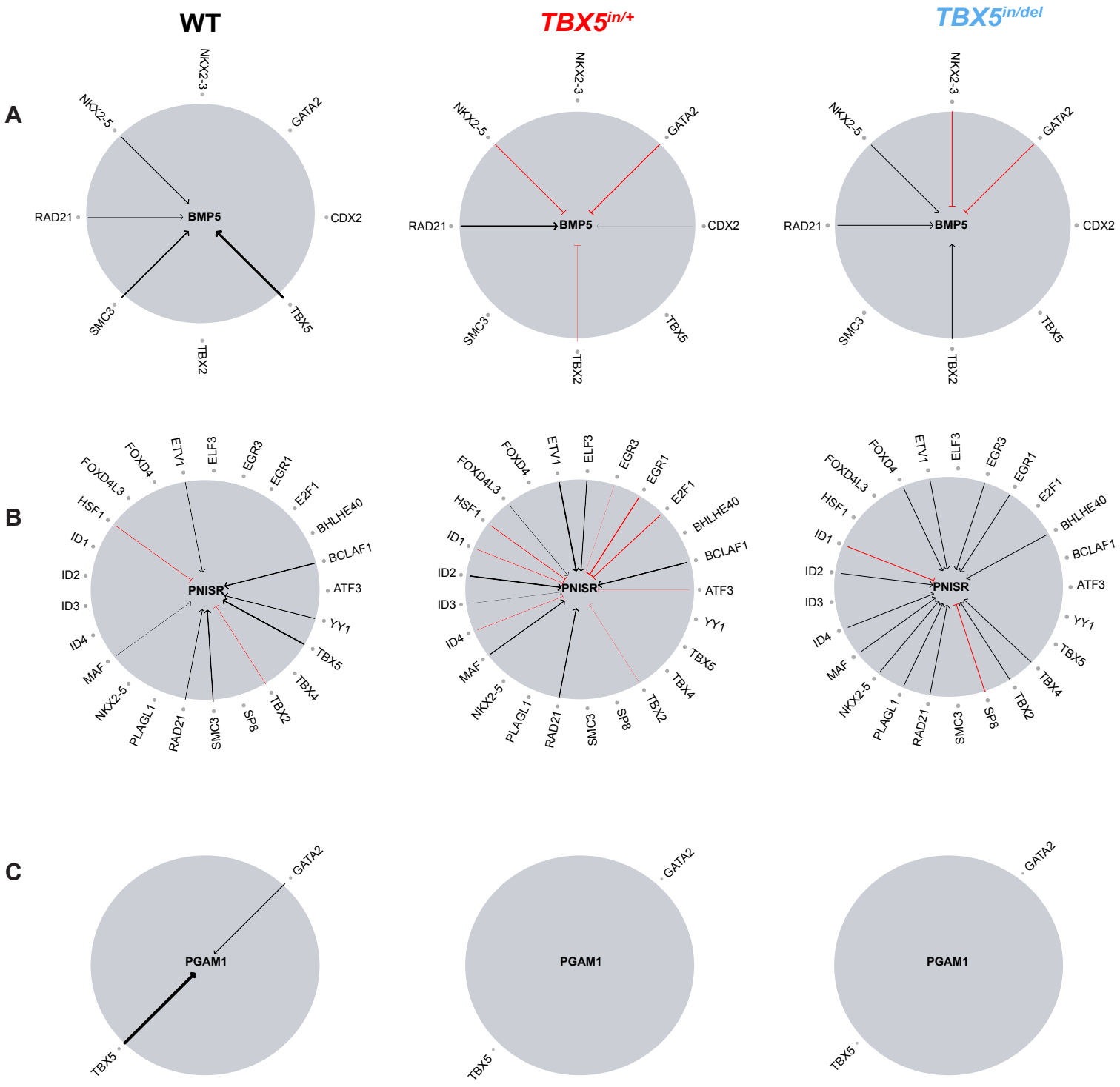
WT
TBX5in/+
TBX5in/del
A
NKX2-3
GATA2
CDX2
TBX5
TBX2
SMC3
RAD21
NKX2-5
BMP5
B
ETV1
ELF3
EGR3
EGR1
E2F1
BHLHE40
BCLAF1
ATF3
YY1
TBX5
TBX4
TBX2
SP8
SMC3
RAD21
PLAGL1
NKX2-5
MAF
ID4
ID3
ID2
ID1
HSF1
FOXD4L3
FOXD4
PNISR
C
GATA2
TBX5
PGAM1